



**National and Kapodistrian University
of Athens**

**Implicit large eddy simulation of a
model ocean surface stratified
turbulent Ekman layer**

A thesis submitted in fulfillment of the requirements for the degree
of Master of Science

in the

**Oceanography and Management of the Marine Environment MSc
Ocean Physics And Modelling Group**

Author

Tilemachos Bolioudakis

Supervisor : Sarantis Sofianos

Advisory Committee : Peter J. Diamessis, Maria Tombrou-Tzella

DECLARATION

I hereby confirm that I have written the present work independently and that I have not used any sources other than those given in the bibliography.

All passages that are taken verbatim or analogously from published or not yet published sources are identified as such.

The drawings or images in of this work have been created by me or provided with a corresponding source reference.

This work has not yet been submitted in the same or a similar form to any other examination authority.

Athens, 21. June 2021

Tilemachos Bolioudakis

ABSTRACT

In the present study, through use of parallel high-resolution/accuracy implicit Large-Eddy Simulation (LES), we examine the development of turbulence and its impact on the vertical structure of background stratification and sheared currents, which have been established through interaction with rotation in the oceanic near-surface zone. Inspiration for the problem set-up has originated from large-scale regional ocean model results and the associated turbulent mixing parameterization. The simulations rely on a high-accuracy hybrid modal-spectral-element/Fourier method incompressible Navier-Stokes flow solver. One of our main goals is to validate this code on a new HPC platform, and, to accurately reproduce and initialize a theoretical Ekman spiral projected on a 3-dimensional domain. Through a selective exploration of parameter space, simulations investigate the impact of stratification on a complex Ekman-spiral-driven turbulent velocity field, including both qualitative and quantitative metrics. The physical time of each simulation is 40 minutes. The computational domain consists of a horizontally-periodic cubic box characterized by $2\pi m$ length in every direction. Analysis of results focuses on comparing scale-dependent turbulent processes of one unstratified and one stratified case, based on flow structure visualization and on monitoring the associated kinetic energy evolution. Finally, a discussion on extrapolating the findings to the oceanic scales is conducted.

Περίληψη

Στην παρούσα μελέτη, μέσω της χρήσης παράλληλης υψηλής ανάλυσης / ακρίβειας implicit Large Eddy Simulation (ILES), εξετάζουμε την εξέλιξη της τυρβώδους ροής και τον αντίκτυπό της στην κατακόρυφη δομή της διαστρωμάτωσης και των ρευμάτων διάτμησης του περιβάλλοντος, τα οποία έχουν δημιουργηθεί μέσω αλληλεπίδρασης με την πλανητική περιστροφή στην επιφανειακή ωκεάνια ζώνη. Η έμπνευση για τη εγκατάσταση του προβλήματος προήλθε από τα αποτελέσματα που παράγονται από τα μεγάλης κλίμακας περιφερειακά ωκεάνια μοντέλα και από τη σχετιζόμενη παραμετροποίηση της τυρβώδους ανάμιξης. Οι προσομοιώσεις βασίζονται σε μια υψηλής ακρίβειας υβριδική μέθοδο-φασματικών-στοιχείων / Fourier, σε ασυμπιεστή Navier-Stokes ροή. Ένας από τους κύριους στόχους μας είναι η επικύρωση αυτού του κώδικα σε μια νέα πλατφόρμα HPC και, η ακριβής αναπαραγωγή και αρχικοποίηση μιας θεωρητικής σπείρας Ekman που προβάλλεται σε έναν τρισδιάστατο τομέα. Μέσω μιας επιλεκτικής εξερεύνησης του χώρου παραμέτρων, οι προσομοιώσεις διερευνούν τον αντίκτυπο της διαστρωμάτωσης σε ένα σύνθετο τυρβώδες πεδίο ταχύτητας που βασίζεται στη σπείρα του Ekman, συμπεριλαμβανομένων τόσο ποιοτικών όσο και ποσοτικών μετρήσεων. Ο φυσικός χρόνος κάθε προσομοίωσης είναι 40 λεπτά. Ο υπολογιστικός τομέας αποτελείται από ένα, περιοδικό στην οριζόντια διεύθυνση, κυβικό κουτί που χαρακτηρίζεται από μήκος 2π m σε κάθε κατεύθυνση. Η ανάλυση των αποτελεσμάτων επικεντρώνεται στη σύγκριση των, εξαρτημένων από την εκάστοτε κλίμακα, διαδικασιών τυρβώδους ροής, μίας μη στρωματοποιημένης και μιας στρωματοποιημένης περίπτωσης, με βάση την οπτικοποίηση της δομής της ροής και την παρακολούθηση της σχετικής εξέλιξης της κινητικής ενέργειας. Τέλος, διεξάγεται συζήτηση σχετικά με την μεταφορά των ευρημάτων στις ωκεάνιες κλίμακες.

*Big whorls have little whorls
Which feed on their velocity,
And little whorls have lesser whorls
And so on to viscosity.*
—Richardson, 1922

ACKNOWLEDGMENTS

The present work has been carried out in the framework of the research activities of the **Ocean Physics And Modelling Group** at the **National and Kapodistrian University of Athens**. Regarding my dissertation, I would like to thank people that via their help, they became the stepping stone to success.

At this point, I would like to express my sincere gratitude to my supervisor, professor Sarantis Sofianos, who trusted me and gave me the opportunity and the support to study the development of turbulent motions from the point of view of Physical Oceanography.

Moreover, I would like to emphasize my deep appreciation to professor Pete J. Diamessis, for being a constant source of inspiration and for his ongoing guidance and valuable time.

I am also grateful to professor Maria Tombrou-Tzella, who as a member of the advisory committee, was present and willing to help me in my research journey.

Furthermore, I am indebted to the PhD candidate of Cornell University, Nidia Cristina Reyes Gil, and to all members of the Ocean Physics and Modelling Group, for their technical support and useful discussions.

Last but not least, I am thankful to my family and closest friends for their understanding, encouragement and for their general support and faith that led in a vigorously grow of my aspirations.

CONTENTS

I THESIS

1	INTRODUCTION	2
1.1	Motivation	2
1.2	Outline	3
2	THEORETICAL BACKGROUND	4
2.1	Oceanic turbulence	4
2.2	Surface Ekman layer	6
2.3	Reynolds-Average Navier-Stokes Approach	7
2.4	LES Approach	8
2.5	Objectives	10
3	METHODOLOGY	12
3.1	Governing Equations	12
3.2	Coriolis Force	13
3.3	Problem Configuration	14
3.4	Grid Spacing & timestep selection	17
3.5	Initial and Boundary Conditions	18
3.6	Validation	20
4	EXPERIMENTS AND RESULTS	21
4.1	Background velocity profile	21
4.2	Fluctuation field	23
4.3	Relaxation procedure	26
4.4	Unstratified results	27
4.4.1	Flow visualization	27
4.4.2	Quantitative results	32
4.5	Stratified results	34
5	CONCLUSION AND DISCUSSION	40
5.1	Summary & connection with project objectives	40
5.2	Extrapolating the current data set into the ocean	41
5.3	Future work	42

II APPENDIX

	Bibliography	46
--	--------------	----

LIST OF FIGURES

Figure 2.1	Schematic of an overturning eddy on a stratified interface, Thorpe - An introduction to turbulence	4
Figure 2.2	Evolution of a simulated K-H instability to 3D turbulence in snapshots, Smyth et al., 2000	6
Figure 2.3	Structure of the surface Ekman layer. Mean horizontal velocity profile (left), Theoretical horizontal velocity vector forming Ekman spiral (Right). From Cushman-Roisin: Introduction to GFD	7
Figure 2.4	Schematic representation of scales in physical space. Black lines represent the computational grid, while the arrows show the representation of an eddying motion. Red lines show the lengthscale of the eddies that each method can resolve. LES deals with scales smaller than those the RANS can recognize. SGS model is used for even smaller scales than the LES resolution.	9
Figure 2.5	Representation of scales in spectral space. Energy cascade from highly energised large structures to smaller lengthscales. From P.A. Davidson. Turbulence: an introduction for scientists and engineers. Oxford University. Cut-off of the LES is located somewhere between inertial subrange and viscosity-dependend eddies.	9
Figure 3.1	Earth's rotation schematic, Kundu, 2012	13
Figure 3.2	PAPA station, located in 50°07'58.9" N 144°49'33.9"W	13
Figure 3.3	SM, FEM, SEM schematic representation and comparison. Boyd, 1989	15
Figure 3.4	Computational domain. Cubic box characterized by $L = 2\pi$ m. Discretization scheme applied on each direction is shown.	16
Figure 3.5	Exponential filter plots for different filter choices. Function is shown in equation (3.8)	17
Figure 3.6	Schematic of the stages of the simulation. Relaxation refers to the velocity field adaptation. In transition, the density gradient is gradually injected. Main run starts after both procedures.	19
Figure 4.1	u & v profile that form an Ekman spiral. Both values derive from equations (4.1) and (4.2) respectively.	22
Figure 4.2	Mean horizontal velocity (u & v shown in figure (4.1) (left), and the associated Ekman spiral (right)	22
Figure 4.3	Half Gaussian versus hyperbolic tangent multiplicative factors as a function of depth.	23

Figure 4.4	1-D Initial vertical profiles of instantaneous background and perturbations sampled at $x=y=L/2$	24
Figure 4.5	u contours in $xy - plane$ in $z = L/2$ (left), and, in $z = L/8$ (right). We observe a similar pattern without direction preference. Colorbar limits are: $[-6.2, -4.6] \cdot 10^{-3}$ (left), $[2.8, 4.6] \cdot 10^{-3}$ (right)	24
Figure 4.6	u_{total} and $u_{perturbation}$ velocity contours in the $xz - plane$ (top) v_{total} and $v_{perturbation}$ velocity contours in the $yz - plane$ (bottom) Colorbar limits are: $[-0.01, 0.05]$ (top-left), $[-0.05, 0.01]$ (bottom-left), $[-1, 1] \cdot 10^{-3}$ (right)	25
Figure 4.7	w contours in xy -plane(left), and in yz -plane(right). Colorbar: $[-8, 8] \cdot 10^{-4}$ (left), $[-1, 1] \cdot 10^{-3}$ (right)	26
Figure 4.8	Kinetic Energy for two unstratified runs of 20 minutes each, with (red line) and without (black line) relaxation procedure	27
Figure 4.9	u perturbations in 4 different corresponding depths. Obvious direction preference is shown, compared to initial state (figure 4.5). Top-left $z=0.79m$, Top-right $z=1.57m$, Bottom-left $z=3.14m$, Bottom-right $z=5.24m$ Colorbar limits are: $[-4, 4] \cdot 10^{-3}$ (Top-left), $[-1.5, 1.5] \cdot 10^{-3}$ (Top-right), $[-5, 5] \cdot 10^{-4}$ (bottom-left), $[-6, 6] \cdot 10^{-5}$ (bottom-right)	28
Figure 4.10	Contours of u in $xz - plane$ (top) and v in $xz - plane$ (bottom) in $y=\pi$ m. Left figures correspond to $t_1 = 600s$, right figures to $t_2 = 2400s$. Colorbar min & max are: $[-0.005, 0.04]$ (top), $[-0.05, 0.005]$ (bottom)	29
Figure 4.11	Contours of u (top) & v (bottom) (xy -plane, $z=2m$). $t_1=600s$ (left), $t_2=2400s$ (right) Colorbar limits are: $[-1, 1] \cdot 10^{-2}$	30
Figure 4.12	W contours in xy -plane ($z=0.79m$ (top), $z=\pi m$ (bottom)). Colorbar limits are $[-2, 2] \cdot 10^{-4}$ everywhere except from (top-right), where min & max are: $[-8, 8] \cdot 10^{-4}$	30
Figure 4.13	Contours of W in xz -plane (top), in yz -plane (bottom). Colorbar limits are: $[-20, 10] \cdot 10^{-5}$ (left), $[-2, 1.5] \cdot 10^{-4}$ (middle), $[-6, 6] \cdot 10^{-4}$ (right).	31
Figure 4.14	Z -vorticity for $z=1.57$ (top), $z = \pi$ (bottom). Colorbar limits are: $[-1, 1] \cdot 10^{-2}$ (top), $[-1, 1] \cdot 10^{-2}$ (bottom-left), $[-5, 5] \cdot 10^{-3}$ (bottom-right)	31
Figure 4.15	Total & mean kinetic energy (left), Mean & perturbations kinetic energy (right)	33
Figure 4.16	Total kinetic energy spectrum in x -direction. $t=0s$ (top-left), $t=600s$ (top-right), $t=1200s$ (bottom-left), $t=2400s$ (bottom-right)	33
Figure 4.17	Total kinetic energy spectrum in y -direction. $t=0s$ (top-left), $t=600s$ (top-right), $t=1200s$ (bottom-left), $t=2400s$ (bottom-right)	34

Figure 4.18	(left) Density profile, x-axis limits are:[1026, 1026.1] (right) Richardson number logarithmic profile, x-axis limits are:[10^{-2} , 10^3]	35
Figure 4.19	Contours of W in xz-plane (top), in yz-plane (bottom). Colorbar limits are: $[-1, 1] \cdot 10^{-4}$ to $[-3, 3] \cdot 10^{-4}$ (left to right).	35
Figure 4.20	W contours in xy-plane ($z=L/10m$ (top), $z=L/2m$ (bottom). Colorbar limits are: $[-8, 6] \cdot 10^{-5}$ to $[-2, 4] \cdot 10^{-4}$ (top - left to right), $[-1, 1] \cdot 10^{-4}$ to $[-6, 6] \cdot 10^{-5}$ (bottom - left to right)	36
Figure 4.21	V contours in xy-plane ($z=L/10m$ (top), $z=L/2m$ (bottom). Colorbar limits are: $[-0.0375, -0.0385]$ (top - left to right), $[0, 12] \cdot 10^{-4}$ (bottom - left to right)	36
Figure 4.22	U contours in xy-plane ($z=L/10m$ (top), $z=L/2m$ (bottom). Colorbar limits are: $[-0.02, -0.015]$ (top), $[-7, -5] \cdot 10^{-3}$ (bottom)	37
Figure 4.23	Z-vorticity contours in xy-plane ($z=L/4$ (top), $z=L/2$ (bottom). Colorbar limits are: $[-1, 1] \cdot 10^{-2}$ (top), $[-1, 1] \cdot 10^{-2}$ to $[-5, 5] \cdot 10^{-3}$ (bottom - left to right)	37
Figure 4.24	ρ' in xz-plane (top), yz-plane (bottom). Colorbar limits are: $[0, 4] \cdot 10^{-7}$ to $[-12, 0] \cdot 10^{-6}$ (top - left to right), $[-2.5, 1.5] \cdot 10^{-7}$ to $[-10, 6] \cdot 10^{-7}$ (bottom - left to right)	38
Figure 4.25	ρ' in xy-plane in $L/10$ (top), $L/2$ (bottom). Colorbar limits are: $[-3, 3] \cdot 10^{-7}$ to $[-1, 1] \cdot 10^{-6}$ (top - left to right), $[-2, 2] \cdot 10^{-7}$ to $[-5, 5] \cdot 10^{-7}$ (bottom - left to right)	38
Figure 4.26	Mean-kinetic energy (left), Perturbations-kinetic energy (right). Comparison between unstratified (red line) and stratified case (blue line).	39
Figure 4.27	Horizontal K E perturbations (left), Vertical K E Perturbations(right). Comparison between unstratified (dashed line) and stratified case (solid line).	39
Figure 5.1	Velocity profiles (left), Density profile (right) Both are sampled from RANS NEMO model	44

ACRONYMS

ARIS	Advanced Research Information System
NetCDF	Network Common Data Form
CFD	Computational Fluid Dynamics
MLD	Mixed Layer Depth
LES	Large Eddy Simulation
DNS	Direct Numerical Simulation
RANS	Reynolds Average Navier Stokes
NEMO	Nucleus for European Modelling of the Ocean
CFL	Courant Friedrichs Lewy
GFD	Geophysical Fluid Dynamics
K-H	Kelvin Helmholtz
Ri	Richardson number
Re	Reynolds number
Ro	Rossby Number

Part I
THESIS

INTRODUCTION

1.1 MOTIVATION

In the field of physical oceanography, the present study focuses on the investigation of the fluid mechanics in the oceanic surface stratified turbulent Ekman layer. Turbulent motions are ubiquitous in all environmental fluids. In an oceanic surface Ekman layer, wind forcing produces shear that generates turbulent flow, impacting the mixing of any stably stratified layers. Vertical mixing plays an essential role in ocean dynamics, as it controls the seasonal stratification profile and it must therefore be correctly estimated. One main objective of ocean modeling is to understand in depth the mechanisms that define turbulent mixing and, in this particular context, the relationship between Ekman dynamics with the variability of the mixed layer depth. The mixed layer is an oceanic surface layer in which active turbulence has homogenized the temperature and salinity (and therefore the density), until the density is fairly uniform. The Mixed Layer Depth (MLD) plays a very important role in the energetic exchanges between the ocean and the atmosphere, as well as in associated biogeochemical processes (Reffray et al., 2015). On one hand, large-scale ocean circulation models usually parameterize the dynamics of the stratified Ekman layer, taking advantage of different turbulent closure schemes (Pollard et al., 1973, Price et al., 1986, Price et al., 1999, Large et al., 1994, Li et al., 2019). On the other hand, the deepening of an Ekman-spiral-driven turbulent layer into a stratified layer has been investigated in small-scale laboratory and high-resolution numerical studies (Zikanov et al., 2003, Pham et al., 2017). A crucial challenge for ocean scientists is, not only to understand the fundamental physics of stratified turbulence but also correctly parameterize it for use in large-scale circulation models (Diamessis et al., 2005, Peters et al., 1988). Therefore, motivated by both Ekman-spiral-driven turbulence, the present study focuses on investigating the entrainment of turbulence and its effect on the stratification, through a high accuracy three-dimensional turbulence-resolving simulation, using a spectral element method / Fourier-Galerkin multidomain incompressible Navier-Stokes solver. Moreover, an opportunity arises for velocity vertical profiles to be compared thoroughly between a Large Eddy Simulation and a Reynolds Average Navier-Stokes simulation, as long as applied the same boundary and initial conditions. The initialization set up of the LES originates from a theoretical Ekman profile similar to the one in Zikanov et al., 2003.

1.2 OUTLINE

Whereas this chapter aims to provide an introduction of the present study, in the next chapter (2), the necessary theoretical background is provided. The Ekman dynamics localized in the upper water column and the related turbulent motions that appear, as well as the main modelling approaches, are introduced in separate sections. The ocean interacts with the wind created in the atmospheric boundary layer via its surface stratified layer. Due to the shear in the vertical, turbulence occurs and plays an important role in mixing. The traditional method to handle turbulent mixing is through parameterizations, as applied in the RANS large-scale ocean modeling. The DNS/LES approach aims to fully or partially resolve turbulence.

In the third chapter, the methodology of the study is reported in detail. The computational domain and the time discretization scheme is defined. Moreover, the time step and the computational grid in 3-dimensional space is generated, in respect to the CFL criterion. The governing equations are mentioned in a non-dimensional form. An extended discussion about the incorporation or not of the Coriolis force is conducted. Regarding the initialization of the simulation process, the initial conditions and the interpolated method used, as well as the conditions that fit the boundaries, are reported. Last but not least, in this chapter, the necessary information that explains the validation process of the code in the National High-Performance Computing facility A.R.I.S, is included.

In chapter 4, the creation of the initial conditions, as well as each simulation setup is included. In these sections, there are clearly noted any differences between the simulations conducted. Furthermore, chapter 4 contains every aspect that affected each model formulation and the results of every simulated setup are cited. The parameters of interest of each case are described, examined, compared and evaluated.

Finally, chapter 5 consists of a summary of the study, as well as a conclusion of the findings. As the present work is an early attempt to initialize an idealized case, future work for transforming results from a large-scale model into a large eddy simulation initial field, is strongly recommended.

THEORETICAL BACKGROUND

2.1 OCEANIC TURBULENCE

Turbulence is generally defined to be an energetic, rotational, and eddying state of motion that results in the dispersion of material and the transfer of momentum, heat, and solutes at rates far higher than those of molecular processes alone. Back in 1895, Osborne Reynolds was the first to recognize that an essential feature of turbulence is that its eddying motions transport momentum. Moreover, the dissipation of energy is one of the most important functions of turbulence in the ocean and is most often used as a measure to characterize it (Thorpe, 2005). Turbulent motions occur in the ocean on scales ranging from millimeters to hundreds of kilometers. The kinetic energy of turbulent motion is spread over a broadband of length or wavenumber scales. Energy is injected in the large scales and transferred to smaller scales. The smallest scales are responsible for the dissipation of energy and mixing as well. Length scales are typically the characteristic diameter of coherent vortical motions, often termed "eddies". In a stratified ocean, turbulent eddies must raise dense fluid above less dense fluid to overturn. In this procedure, as shown in figure 2.1, kinetic energy is converted to potential energy and vice-versa.

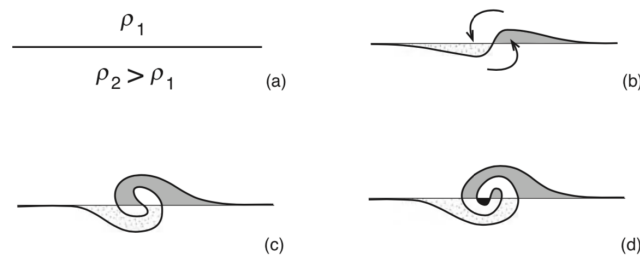


Figure 2.1: Schematic of an overturning eddy on a stratified interface, Thorpe - An introduction to turbulence

In the near-surface layer of the ocean, the main sources of turbulence are background shear, breaking surface waves, internal waves, Kelvin - Helmholtz instability, and convection (Soloviev, 2006). Shear is the spatial gradient of the velocity in a direction normal to its direction. Both shear and convergence (or divergence) are inherent in the three-dimensional eddying motion of the turbulent flow.

Generally, there are two fundamental non-dimensional parameters that are necessary to take into account when dealing with turbulence. At first, the Reynolds number (Re) characterizes the transition from laminar flow to turbulent. Furthermore, the Richardson number (Ri) describes the con-

ditions necessary, but not sufficient, for a stably stratified shear flow to be unstable, allowing small disturbances in a finite band of wavenumbers to grow, known as Kelvin – Helmholtz instability (Thorpe, 2007). K-H instability produces overturning billows, that can occur only when the gradient Richardson number is less than its critical value somewhere in the flow. This is known as the Miles–Howard theorem. It is essential to highlight that, Ri lower than the critical value does not necessarily imply the birth of turbulence. Both parameters and their critical values may be formally defined as:

- $Re = \frac{U \cdot L}{\nu}$, where U describes the velocity, L the length and ν the viscosity. The critical value for a flow to be considered turbulent is $Re_{critical} \geq 1000$.
- $Ri = (\frac{N}{S})^2$, where N is the buoyancy frequency ($N^2 = -\frac{g \cdot \partial \rho}{\rho \cdot \partial z}$) and S is the shear ($S = \frac{dU}{dz}$) (assuming that the background is not varying in x, y). The critical value is $Ri_{critical} \leq \frac{1}{4}$.

In general, in a parallel shear-driven stratified flow, 2-dimensional K-H instability can be developed. During this process, overturning billows are being formed. The billows grow and develop pairs of vortices that will usually produce convective rolls. At this stage, relatively small-scale internal motions develop within the billows, their early stages being regular and spatially periodic, though rapidly becoming disorganized, three-dimensional, and turbulent. The turbulent patches, still retaining the vestiges of periodicity of the billows, become elongated in the flow direction, resulting in a layer of turbulence containing small-scale density fluctuations. Turbulence eventually subsides, leaving a layer thicker than the original interfacial layer (Thorpe, 2007). This procedure is shown in figure (2.2). This is the canonical scenario, yet in this study, we will not investigate this progressive transition to turbulence.

In this study, we localize our interest in the examination of turbulent events in the upper ocean. K - H instability does not appear clearly somewhere in the flow, as we use the “bypass transition to turbulence” technique in our simulations (Jacobs et al., 2001, Voke et al., 1995). In this way, we assume that a turbulent state of motion is already present in our flow, without following the step-by-step transition that described above.

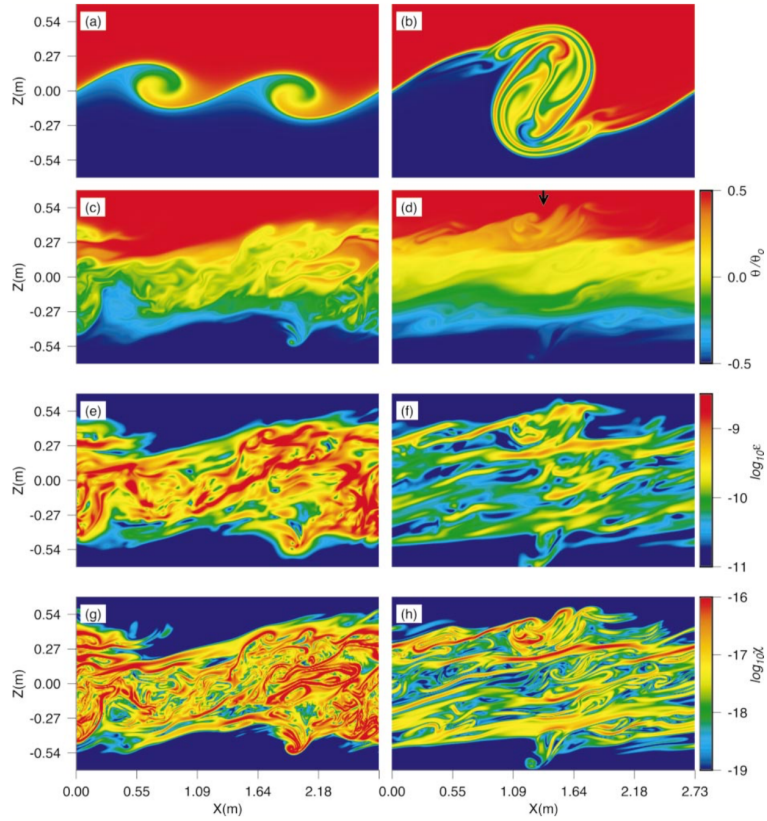


Figure 2.2: Evolution of a simulated K-H instability to 3D turbulence in snapshots, Smyth et al., 2000

2.2 SURFACE EKMAN LAYER

Upper-ocean turbulence resulting from shear and convection may be substantially influenced by the diurnal cycle of solar radiation and precipitation events. The upper-ocean boundary layer includes the sea surface and its wave field, the mixed layer, and the upper part of the pycnocline. The thickness of this layer is not fixed and is directly affected by the atmosphere.

An Ekman layer occurs wherever there is horizontal frictional stress, such as, in our case, along the ocean surface, where waters are subject to wind stress (Cushman-Roisin et al., 2011). This specific phenomenon, first studied by Ekman in a historic paper in 1905. In these layers, mean flows spiral in direction as the surface boundary is approached, a consequence of Coriolis and frictional forces. The Ekman layer currents form a spiral-shaped profile in which the current vector decays and rotates to the right with increasing depth. In the following figure, we visualize the x - z plane of u and v components (left), as well as a three-dimensional representation of the mean horizontal velocity vector through the z -axis, as presented in Cushman-Roisin.

However, reality seems to diverge a little bit from theory. There are three main observational factors that account for substantial differences: turbu-

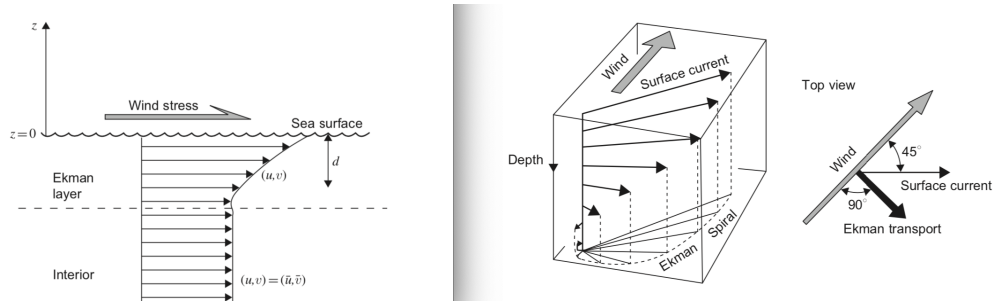


Figure 2.3: Structure of the surface Ekman layer. Mean horizontal velocity profile (left), Theoretical horizontal velocity vector forming Ekman spiral (Right). From Cushman-Roisin: Introduction to GFD

lence, stratification, and horizontal gradients. The dramatic effect of stratification is observed under low wind speed conditions when the turbulence regime depends strongly on near-surface stratification, while the strong stratification is also the result of reduced turbulent mixing (Soloviev, 2006). The observed spirals differ mainly in their thickness. They have a shape that is somewhat similar to that of a classical Ekman spiral, while the difference in detail is that, compared to a classical Ekman spiral, the velocity decreases with depth more rapidly than the current vector rotates to the right and these spirals appear to be flattened or compressed in the downwind direction (Price et al., 1999)

2.3 REYNOLDS-AVERAGE NAVIER-STOKES APPROACH

Turbulent flows can be characterized as somewhat random fluctuations of the flow variables; rapid diffusion due to mixing; three-dimensional turbulent structures due to vorticity, i.e., eddies; dissipation of energy and vorticity; non-linearities (Kundu, 2012). The Reynolds averaged Navier–Stokes (RANS) equations usually are being employed in numerical simulations that do not resolve turbulence, they strictly parameterize it, and, aim to produce results at a reasonable and time-efficient computational cost. The reference equations can be defined by applying the Reynolds decomposition, such as using in the momentum equation two velocity components: one mean profile and one that describes a temporal, lower in order perturbation. In the RANS momentum equation, special attention must be paid to additional terms resulting from fluid velocity (Wu et al., 2019). In the light of the momentum exchange within fluid layers due to turbulence, these terms can be interpreted as Reynolds stresses (Windt et al., 2020). The occurrence of additional terms in the RANS momentum equations contain unknown variables and requires additional equations to achieve closure of the system of equations. This problem is known as the Turbulence Closure Problem. These additional equations can be provided in the form of turbulence closure models, and make use of additional algebraic or differential relations. The type of closure

(algebraic or differential) and the number of auxiliary equations defines the closure level (Hanjalić, 1994).

In large-scale ocean modeling, the turbulence issue raises the question of how to compute accurately the associated vertical turbulent viscosity and diffusivity (Reffray et al., 2015). Eddy coefficients are commonly used in providing a parameterization of turbulent fluxes, with the eddy diffusion coefficient times the gradient of the transferred quantity being equal to the turbulent flux, i.e. the Reynolds stress. More specifically, there are many ways of computing these eddy coefficients that are related to different turbulent closure schemes. The method identified as one of the most applied turbulence models in the literature is known as the "General Length Scale" scheme that includes "k- ϵ ", "k- ω and "Mellor-Yamada" models (Mellor et al., 1982, Umlauf et al., 2005). It is also usually used the approach of "Turbulence Kinetic Energy" and the "Richardson dependent" closure scheme (Cuxart et al., 2000). For validating and calibrating these turbulence models, the Kato-Phillips (Kato et al., 1969) laboratory experiment is classically used (Deleersnijder et al., 2008). Regarding the applied resolution of scales, all the different closure schemes referred to above, do not have the ability to directly recognize and resolve turbulence. As a result, the numerical approach that someone will choose usually is guided by the scope of the study and the associated resolution of scales needed. In this study, we aim to resolve a great variety of turbulent scales, and, as a consequence, we will not use RANS.

2.4 LES APPROACH

Numerical simulation of turbulence is an extremely complicated task, characterized by very high numbers of degrees of freedom. When in need of high accuracy in resolving turbulence from the point of view of computational fluid dynamics, more complex approaches can be applied. Direct numerical simulation (DNS) or large eddy simulation (LES) are more detailed but more costly approaches to consider turbulence in numerical modeling. The resolution of scales in both LES / DNS approaches is far better than in RANS, where the mesh that is applied cannot recognize and resolve the turbulent spatial scales. LES is situated somewhere between the DNS and the RANS approach, as the larger domain eddies are directly resolved, while smaller eddies are parameterized. More specifically, the RANS approach in the ocean is based on statistical averaging that leads to steady, 2-dimensional equations (where the third direction is described by hydrostatic balance), while LES is based on local filtering, where the equations are unsteady and 3D. The filtering operation on the flow variables introduces a technique that resolves large scales of the motion and only the repercussions of the small ones needs to be modeled. DNS tend to resolve in detail all scales bigger than molecular scales. In the next figure (2.4), there is a representation in the physical space of the different scales that can be directly resolved in a RANS or LES model.

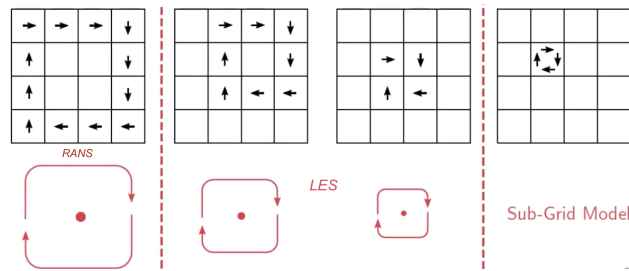


Figure 2.4: Schematic representation of scales in physical space. Black lines represent the computational grid, while the arrows show the representation of an eddying motion. Red lines show the lengthscale of the eddies that each method can resolve. LES deals with scales smaller than those the RANS can recognize. SGS model is used for even smaller scales than the LES resolution.

As referred in the introduction, turbulent flows are characterized by vortices with a wide range of spatial and temporal scales. The interaction between these different-scale vortices transfers the mean square vorticity to higher wavenumbers as time passes, an evolution known as ‘cascade of energy’. A crucial factor for this section is to clarify in detail the relation between the scales of energy and wavenumbers magnitude. For this purpose, the above scales in wavenumber space and their dependence of energy content of turbulent motions, are presented here, in a homogeneous and isotropic turbulent flow. The diagram below (figure 2.5), is a great contribution to the work of many famous scientists, such as Andrey Kolmogorov and Geoffrey Ingram Taylor.

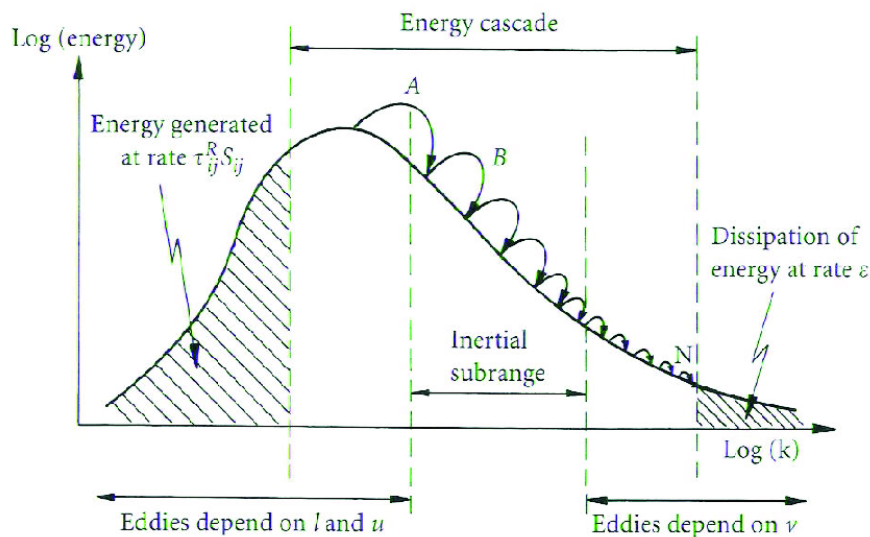


Figure 2.5: Representation of scales in spectral space. Energy cascade from highly energised large structures to smaller lengthscales. From P.A. Davidson. Turbulence: an introduction for scientists and engineers. Oxford University. Cut-off of the LES is located somewhere between inertial subrange and viscosity-dependent eddies.

Hence, in most cases, LES explicitly deals with the eddies of turbulent motion of a fluid that are most energetic. In the range of higher wavenumbers that contain less amount of energy, there is usually a Subgrid Scale model used for the coupling of the resolved and unresolved scales. In our study, we make use of the Implicit Large Eddy Simulation (ILES) (Diamessis et al., 2011). In this case, the effects of small scales that cannot be resolved directly on the LES mesh are represented by a different approach, in contrast with the SGS model, that was initially proposed by Boris et al., 1992. In explicit LES, an SGS model is usually used to resolve the dissipative scales as a way to overcome the restrictions in available computer resources. The implicit LES approach is based on the observation that truncation errors in certain discretizations of Navier–Stokes equations introduce numerical dissipation with the implicit effects of the discretization qualitatively similar to the effects of the explicit SGS models in traditional LES (Diamessis et al., 2011). Alternatively, if one uses a higher order method (e.g. spectral) the, explicitly controlled, numerical dissipation is provided by either spectral filtering or use of hyperviscous operator. Details of this method and its applications are given by Fureby et al., 2002. The simulations presented herein may be viewed as a spectral implicit LES, based on high order methods, where the stabilization is not provided by the truncation error of the numerical discretization, but by the spectral filter (Diamessis et al., 2011). For the purposes of this study, a flow solver that consists of a hybrid Fourier/Spectral-Element spatial discretization of the incompressible Navier-Stokes equations under the Boussinesq approximation is employed. The code mentioned is a modified version of the code that was originally created by Professor P.J. Diamessis and used in the publication of "Diamessis et al., 2005". In the updated version of the code, there is a transition to modal spectral element methods in the vertical direction. In the next chapter, the governing equations are presented, as well as the domain setup used.

2.5 OBJECTIVES

In this section, the objectives of the research project are provided. First of all, one of our main goals is to validate the code on a new HPC platform, and, simulate an idealized case in order to gain confidence in investigating an Ekman layer that derives from the RANS simulation, in the future. Furthermore, we attempt to accurately reproduce and initialize a *theoretical Ekman spiral* projected on a 3-dimensional domain. This idealized case takes place in a small-size computational domain, and any potential to extrapolate the findings to the oceanic scales is discussed in section (5.2). We insist on constructing the most suitable initial state, based on the complex Ekman velocity field. Moreover, we analyze and compare the results of one unstratified and one stratified case. The analysis includes both

qualitative and quantitative metrics. On the one hand, we visualize the velocity, density, and vorticity field. On the other hand, we calculate the kinetic energy of the mean profile, as well as of the perturbation fields. Overall, the present study focuses on setting up and validating a simple implicit Large Eddy Simulation, that is necessary in order to pursue our initial, broad research goals (mentioned in section 5.1), in the future.

METHODOLOGY

3.1 GOVERNING EQUATIONS

The equations governing the problem investigated are the 3-dimensional incompressible Navier–Stokes equations under the Boussinesq approximation (Diamessis et al., 2011). The system of these equations for a turbulent flow field can be written in the following form:

$$\frac{\partial \mathbf{u}}{\partial t} + \frac{1}{2}[\mathbf{u} \cdot \nabla \mathbf{u} + \nabla(\mathbf{u} \cdot \mathbf{u})] = F_g + F_c - \frac{1}{\rho_0} \nabla p' + \nu \nabla^2 \mathbf{u} \quad (3.1)$$

$$\text{where,} \quad F_g = -g \frac{\rho'}{\rho_0} \hat{\mathbf{k}} \quad , \quad F_c = -2\Omega \times \mathbf{u} \quad (3.2)$$

$$\nabla \cdot \mathbf{u} = 0 \quad (3.3)$$

$$\frac{\partial \rho'}{\partial t} = -\nabla \cdot (\mathbf{u}(\rho' + \bar{\rho}(z))) + \kappa \nabla^2 \rho' \quad (3.4)$$

A right-handed coordinate system is used, where x points to the east, y points north, and z points up. The equation (3.1) represents the Navier-Stokes in 3 dimensions, as \mathbf{u} is the velocity vector : $\mathbf{u} = (u, v, w)$. Moreover, the non-linear term in equation (3.1) is written in the skew-symmetric form to minimize aliasing effects in the numerical solution (Boyd, 1989). In equation (3.2), there is the gravity force, with $\hat{\mathbf{k}}$ the normal unit vector in the vertical direction. The F_c term represents the Coriolis force. In equation (3.3) is the continuity equation. In equation (3.1), we use the pressure perturbation p' and in equation (3.4), the density perturbation q' , from their respective (mean) reference values. Both originate from a decomposition of their corresponding total values, as:

$$p = \bar{p}(x, y, z) + p'(x, y, z, t) \quad (3.5)$$

$$\rho = \rho_0 + \bar{\rho}(z) + \rho'(x, y, z, t) \quad (3.6)$$

Last but not least, under the Boussinesq approximation, the reference pressure and density are in hydrostatic balance:

$$\frac{\partial \bar{p}}{\partial z} = -(\rho_0 + \bar{\rho}) \cdot g \quad (3.7)$$

3.2 CORIOLIS FORCE

At this point, one must necessarily include an extended discussion about the Coriolis force. The Coriolis force is equal to the product of the Coriolis parameter (f) and the horizontal velocity component. More specifically, $F_c = f \cdot v$ in the x -direction, and $F_c = -f \cdot u$ in the y -direction. The Coriolis parameter (or frequency, as many times referred to in the literature) varies with latitude θ ($f = 2\Omega \sin(\theta)$), where Ω is the Earth's rotation frequency and θ is the latitude).

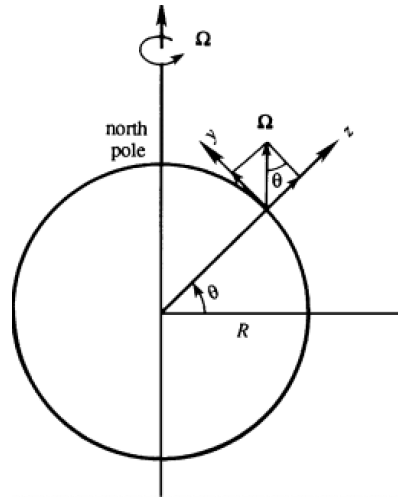


Figure 3.1: Earth's rotation schematic, Kundu, 2012

However, this variation is important only for phenomena having very long time scales (several days to weeks) or very long length scales (hundreds to thousands of kilometers). For many purposes, we can assume f to be a constant, say $f_0 = 2\Omega \sin(\theta_0)$, where θ_0 is the central latitude of the region under study (Kundu, 2012). In this study, we assume that our idealised case is situated in the North Pacific, where the NOAA PAPA buoy lays (for comparison with results sampled from a RANS model, in future work). As a consequence, we compute $f_0 = 1.114 \cdot 10^{-4} \text{s}^{-1}$.

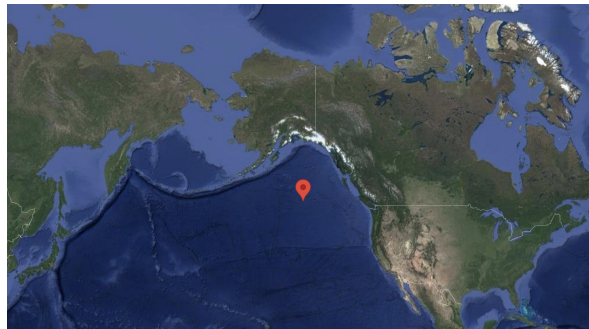


Figure 3.2: PAPA station, located in $50^{\circ}07'58.9''$ N $144^{\circ}49'33.9''$ W

The Coriolis parameter plays an important role in the formation of the surface Ekman layer. More broadly, the Coriolis parameter affects the depth

of the Ekman spiral and layer as well ($D_{Ekman} \sim \sqrt{\frac{A_v}{f}}$, A_v represents the eddy viscosity and diffusivity parameter, vertically). However, the spatial scale of the domain under review ($\sim 6m$), as well as the temporal scales of our study ($\sim 40min$), lead us to the conclusion that in our simulations, that have initialized with a predefined Ekman spiral, water particles do not have the ability to feel the Coriolis effect. In this study, we include phenomena so rapid that, after a temporal scaling in the Navier-Stokes equations there is no reason to take its effect into account. The above conclusion is easily explained, using another non-dimensional parameter; Rossby number.

- $Ro = \frac{U}{Lf}$, where U represents the scale of the velocity, f the Coriolis frequency and L the length scale of the phenomenon under review

Ro is an index that shows the importance of timescales between gravity and rotation. The critical Ro value, where gravity timescale is equal to rotation, is obviously $Ro \sim 1$. In our idealized case, we make use of a maximum velocity $\simeq 0.05 m/s$ in a domain length $\sim 2\pi m$, that results in a $Ro \sim 100$. It is clear that gravity and the associated non-linear effects dominate over rotation. As a result, the contribution of the Coriolis force is so small that can be ignored without the simulation discussed here generating any spurious physics.

3.3 PROBLEM CONFIGURATION

The accuracy of a numerical simulation is highly contingent on the choice of numerical discretization. The types of numerical discretizations of the time-dependent, incompressible Navier-Stokes equations are varied and widely formulated (Durrant, 2010, Ferziger et al., 2020). Generally speaking, the main differences among them lie in the time-discretization scheme, the spatial discretization strategies and the algebraic solvers that are used. For the purposes of this study, Fourier-Galerkin spectral discretization and Spectral Element Methods are applied.

In general, SEM are a hybrid of Finite Element Methods and Spectral Methods. FEM use local basis functions of limited degree (1st or 2nd), whereas SM use global basis functions of high degree. In SEM, the domain is subdivided into elements (M), while the degree of the polynomial basis function is P is sufficiently high (Boyd, 1989).

Spectral element discretization provides the most accurate numerical approximation of the governing equations for capturing a great range of scales, while it reduces the operation count and impact of round-off error compared to a single domain computation with the same number of grid points. The most important advantage of the SEM is that, the elements in the vertical direction will be arranged in order to localize resolution in areas of interest. Moreover, SEM minimize the number of diffusion, as the smallest resolved scales are not artificially damped. Furthermore, when one seeks for high accuracy in complex flows, he needs to push up the Re number. SEM use less grid points for representing with same accuracy the related flow, than

a FEM method does. As a result, one can use SEM in order to simulate a higher Reynolds number flow with the same computational cost, as FEM use for a smaller Re. Last but not least, SEM tend to have minimal numerical dispersion.

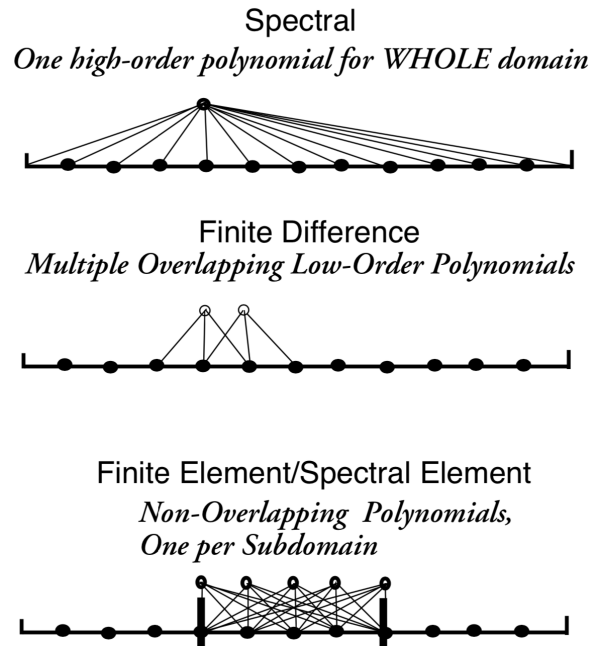


Figure 3.3: SM, FEM, SEM schematic representation and comparison. Boyd, 1989

In this study, the computational domain is a 3-dimensional volume inside an extended Ekman layer region. Within this volume of dimensions $L_x \times L_y \times L_z$, the three-dimensional and time-dependent Ekman flow field is computed. The domain is assumed to be periodic in both horizontal directions.

The computational domain is chosen to represent an oceanic cubic box with $L=6$ m. In both zonal and meridional directions, a Fourier-Galerkin spectral discretization is used. The total number of grid points in each horizontal direction is chosen in such a way as to secure a resolution of less than 10 centimeters. In the vertical direction, modal spectral element methods are applied. The domain is partitioned into M subdomains of variable height, while within each subdomain, Legendre-Lobatto polynomials with fixed order P are used. Subdomains communicate with their neighbors via a simple patching condition. Between two elements, there is a fixed number of nodes Q . The total number of vertical nodes in physical space is $N_z = M(Q - 1) + 1$. This amount of nodes ensures a vertical resolution finer than 10 centimeters in the localized areas of interest, confirmed by the vulnerable-thickness elements.

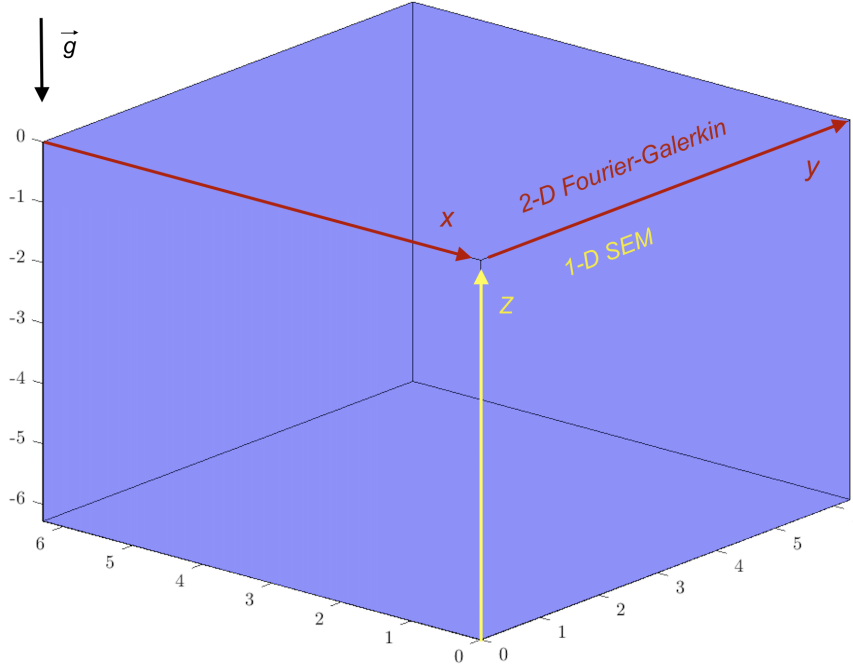


Figure 3.4: Computational domain. Cubic box characterized by $L = 2\pi$ m. Discretization scheme applied on each direction is shown.

For the grid resolutions considered in this study, in conjunction with attaining Re values, as close as possible, of true oceanic conditions in our simulations, we are in need of a strategy that ensures stability in the numerical solution. In our case, we apply a low-pass spectral filter on the numerical solution. In practise, an exponential filter that is shown below, is used, in order to provide sufficiently stable numerical solution. The use of the filter consists of a highly advantageous way of introducing the dissipation needed for stabilization (Hesthaven et al., 2008), which bypasses the numerical stiffness associated, by using a hyperviscous operator in the vertical. The filter transfer function is defined as:

$$\sigma(k) = \begin{cases} 1, & \text{if } 0 \leq k \leq N_c \\ \exp[-a(\frac{k-N_c}{N-N_c})^s], & N_c \leq k \leq N, \end{cases} \quad (3.8)$$

where s is the filter order, N_c the filter lag and $a = -\ln \epsilon_m$ with ϵ_m being the machine precision. In Legendre space, k and N represent the mode number and total number of available modes, respectively. In Fourier space, k and N represent the two-dimensional wavenumber vector magnitude and the corresponding maximum value over all resolved horizontal wavenumbers, respectively (Diamessis et al., 2011). In the next figure (3.5), examples of different order filters are shown. As shown in the figure, this study uses $N_c = 0$.

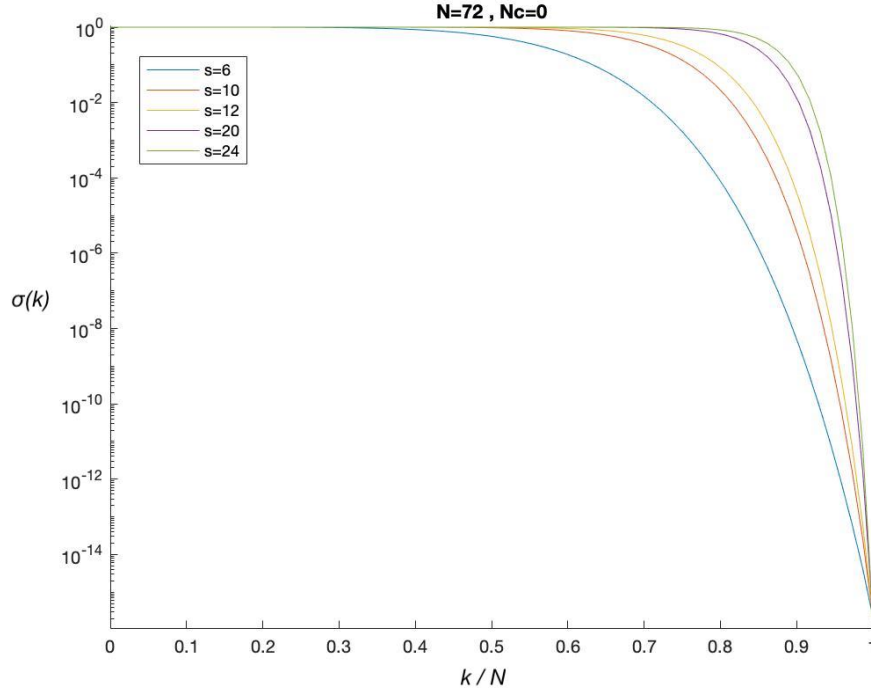


Figure 3.5: Exponential filter plots for different filter choices. Function is shown in equation (3.8)

In the incompressible spectral Fourier / SEM solver presented in this study, spectral filtering is applied in all three directions. In equation (3.8), we choose $s = 18$ for the solutions in the horizontal directions, and, $s = 12$ for those in the vertical. For the Re under consideration, use of spectral filtering is the inevitable price when confronted with the associated high-degree of under-resolution (see next section of actual values of grid spacing). Filtering should not be viewed as a waste of resolution because a significant percentage of modes of the numerical solution are not directly affected by the filtering procedure. The filtered modes act as a sink of both numerical noise and energy flux from the large scales. Although their content is not necessarily physically correct, their presence is needed to maintain the stability and spectral accuracy of the solution at the larger resolved (physical) scales (Diamassis et al., 2005).

3.4 GRID SPACING & TIMESTEP SELECTION

In both horizontal directions, the number of grid points is $N_x = N_y = N_h = 128$. As a result, for the domain setup discussed above ($L_x = L_y = L_z = L = 6m$), Δx and Δy are both constant and equal to L/N_h . In contrast, Δz is not constant over the whole z-axis, as the elements are placed in such a way that secures the resolution needed to capture a wide range of turbulent scales. In the localized areas of interest, Δz approaches a value less than one

quarter of 1 meter. The computational timestep Δt was chosen as such that the CFL stability criterion is obeyed in all three spatial directions for a 3rd order stiffly stable scheme, in a similar way as applied in Diamessis et al., 2011. The following requirements are imposed:

$$\Delta t \frac{u_{max}}{\Delta x} < 0.2 \quad (3.9)$$

$$\Delta t \frac{v_{max}}{\Delta y} < 0.2 \quad (3.10)$$

$$\Delta t \left[\frac{w}{\Delta z} \right]_{max} < 0.2 \quad (3.11)$$

The time step (Δt) that is computed above in each direction, is characterized by an order of magnitude $\simeq 0.1$ seconds, and, is kept fixed for the whole simulation.

3.5 INITIAL AND BOUNDARY CONDITIONS

The intrinsic sensitivity of a spectral/spectral-element scheme to any assumptions on initial/boundary conditions and forcing (Boyd, 1989) has led to a much more rigorous and careful treatment of simulation initialization than that usually given in the literature (Diamessis et al., 2011). The initial conditions consist of a three-dimensional velocity field, in conjunction with a uniform in x and y direction, z dependent density profile. Following the above discussion, the initial flow field is chosen as the superposition of a mean velocity profile and a turbulent fluctuation field:

$$u(x, y, z, t) = u_{mean}(z, t) + u'(x, y, z, t) \quad (3.12)$$

$$v(x, y, z, t) = v_{mean}(z, t) + v'(x, y, z, t) \quad (3.13)$$

$$w(x, y, z, t) = w'(x, y, z, t) \quad (3.14)$$

The predeveloped field of the velocity perturbations is a result of the "bypass transition to turbulence" approach, mentioned in the previous chapter. A variety of approaches may be found in the literature regarding the specification of the magnitude and distribution of the mean and fluctuating velocity fields. In our setup, the u_{mean} and v_{mean} components, that derive from the same equations presented in Zikanov et al., 2003 (section 4.1 - equations 4.1 & 4.2) are responsible for the Ekman spiral formation (details of the spiral can be found in section 2.2). The initial w_{mean} velocity is set to zero.

The three-dimensional fluctuating velocity field is constructed as spectrally filtered white noise in three-dimensional Fourier space following a $k^{-5/3}$ energy spectrum slope. An inverse Fourier transform is applied to convert the noise into physical space and in the vertical, the fields are projected on the non-uniform Lobatto–Legendre grid of each subdomain. The noise is tested to respect the periodicity of the code at the boundaries and to secure the stability of the numerical solution. The initial conditions were generated in Matlab in netcdf format, and, the windowing of the noise is presented in detail in the next chapter.

Initially, the fluctuating and mean velocity fields are uncorrelated. As a result, the most expected scenario for the turbulent fluctuations would be to evolve independently of the mean and decay after only a few eddy turnover times, beyond which the mean flow decays strictly due to viscous effects. To avoid this behavior, which is caused by the lack of correlation between fluctuating and mean velocity fields, a preliminary ‘relaxation’ simulation (Dommermuth et al., 2002) is run to generate a physically realistic velocity field. During relaxation, the flow is forced to maintain constant mean and fluctuating velocity profiles, while the spatial distribution of the turbulent fluctuations, and thus the Reynolds stresses, is allowed to vary.

An additional preliminary simulation, a ‘transition’ run, is performed, where mean and fluctuating velocity profiles are allowed to adjust. During the transition run, an initial fluctuating density field is generated by the evolving turbulent field in an ambient density gradient (and the Brunt–Vaisala frequency N) that are gradually ramped to the desired value to avoid re-stratification-related transients. The whole procedure of relaxation and transition, shown in the next figure (3.6), is very similar to that applied in Diamessis et al., 2011.

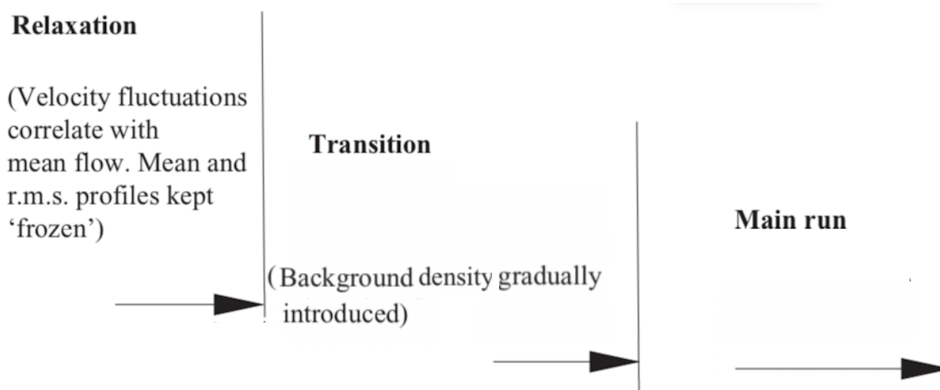


Figure 3.6: Schematic of the stages of the simulation. Relaxation refers to the velocity field adaptation. In transition, the density gradient is gradually injected. Main run starts after both procedures.

The boundary conditions used in the numerical model correspond to the description of the previously discussed computational domain. In the horizontal directions, periodic boundary conditions are employed. In both top and bottom boundaries, a free-slip non-deformable surface condition is ap-

plied for the relaxation and transition stages. In the main code, one is able to choose between the free slip and a constant forcing at the surface. We choose not to use the finite stress boundary condition, due to lack of time to investigate thoroughly some numerical instabilities that appeared. Instead, we used free-slip boundary condition for the velocity field, at both the top and bottom boundaries. Finally, the density perturbation is subject to zero flux ($\frac{\partial \rho'}{\partial z} = 0$) at the vertical boundaries.

3.6 VALIDATION

The installation and implementation of such a code in a new HPC platform has been a challenging task. The setup took place in the National High-Performance Computer A.R.I.S., as we were in need of high memory capabilities and computing power. Keeping in mind that it is the first time that Ekman dynamics will be resolved by this code, it was essential for one to be 100% confident that the code produces exactly the same results compared to previously tested cases. This testing procedure included many benchmark cases. However, only the most significant of them are presented here.

The first method of verification presented here is the vortex dipole experiment (Clercx et al., 2006). In this experiment, we verified that we are able to represent in detail the well-known "Vortex Dipole" in an unstratified 2-dimensional domain, compared to the results of Clercx et al., 2006. We included a qualitative examination of the vortex dipole development, as well as a quantitative comparison, based on time series of kinetic energy and enstrophy.

The second case presented here is the "DJL solitary wave", which is based on the Dubreil-Jacotin-Long equation. The (DJL) equation is derived from the steady, incompressible Euler equations. The result is a single, non-linear equation for the isopycnal displacement. The initial conditions were created in Matlab as in Dunphy et al., 2011. To solve the DJL equation, the pseudospectral numerical method developed by Dunphy et al., 2011 is employed, in a stratified 2-dimensional domain. In this experiment, we verified that the wave maintains constant wave form, fixed propagation speed equal to theoretical value, and, coherent kinetic energy. Our results can be verified by the results presented in Rivera-Rosario et al., 2020.

In our last test case, we successfully tested a stratified 3-dimensional turbulent experiment. In this particular case, the mean velocity profile scaling and the vorticity structure of a stably stratified, initially turbulent wake of a towed sphere, in a predefined $Re = 5000$, was examined. Our results are a successful representation of those presented in Diamessis et al., 2011. The above mentioned benchmarks served as a progressive test procedure that resulted in gaining confidence for setting up our case using the same numerical solver.

EXPERIMENTS AND RESULTS

The simulations set-up follows a progressive procedure: initially creating the background profiles, building the perturbations field, and following a spin-up phase, conducting unstratified and stratified simulations. In this chapter, the details of each simulation that took place are reported. Although there are many approaches on how to compute Re (e.g. Pham et al., 2017), we will use the definition mentioned in section (2.1). In every simulation we will consider $Re \simeq 10^5$, calculated by the maximum velocity $V_{max} = 0.05 \text{ m/s}$ (as shown in the following section), the Ekman-spiral depth as the length scale ($\sim 5\text{m}$), and, viscosity very close to the actual oceanic value, equal to $\nu = 10^{-6} \text{ m}^2/\text{sec}$.

4.1 BACKGROUND VELOCITY PROFILE

As discussed in section (2.2), Ekman assumed a balance between the Coriolis force, viscous friction and the pressure gradient, adopted the approximation of constant vertical eddy viscosity A_z , and derived a solution now known as the ‘Ekman spiral’ (figure 2.3). For the purpose of building this Ekman spiral, we follow a similar procedure as in Zikanov et al., 2003. In the case of a steady wind in the x -direction, the steady-state, surface Ekman velocity profile in the open ocean is (for the northern hemisphere) :

$$u = V_0 \cos\left(\frac{\pi}{4} + \frac{\pi}{D}z\right) \exp\left(-\frac{\pi}{D}z\right) \quad (4.1)$$

$$v = -V_0 \sin\left(\frac{\pi}{4} + \frac{\pi}{D}z\right) \exp\left(-\frac{\pi}{D}z\right) \quad (4.2)$$

The background velocity consists of an one-dimensional, depth-dependent profile for each u and v component, where z represents the vertical coordinate. In addition, $V_0 = \sqrt{2}\pi\tau_0/D\rho_0f$ is the amplitude of the surface velocity, $D = \pi(2A_z/f)^{1/2}$ is the Ekman depth of exponential decay, τ_0 is the surface shear stress, and, f is the Coriolis parameter for the PAPA station (figure 3.2). The surface shear is computed as $\tau_0 = C_d\rho_{air}v_{10}^2$, where $C_d = 1.4 \cdot 10^{-3}$ is the unitless drag coefficient, $\rho_{air} = 1.3 \text{ kg/m}^3$ is the air density, and $v_{10} = 2 \text{ m/s}$ is the wind speed at 10 m. This profile was initially built for a larger domain ($L \sim 120\text{m}$ and $D \sim 80\text{m}$), and then, due to the computational limitation of the flow solver, was finally adapted to our computational domain (figure 3.4). In figure (4.1), the final u and v velocity profiles are shown. In figure (4.2), the mean horizontal velocity as a function of depth, as well as the Ekman spiral produced, are presented.

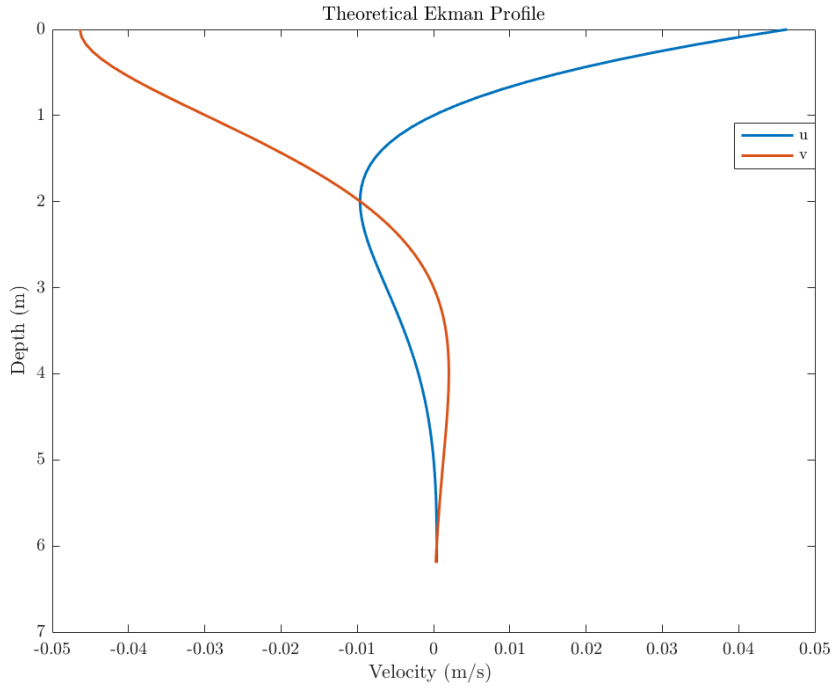


Figure 4.1: u & v profile that form an Ekman spiral. Both values derive from equations (4.1) and (4.2) respectively.

In the next section, in order to generate the initial turbulent velocity field, we are going to overlay an artificially predeveloped spectrally-filtered noise field on the background velocity profile, as explained in section (3.5).

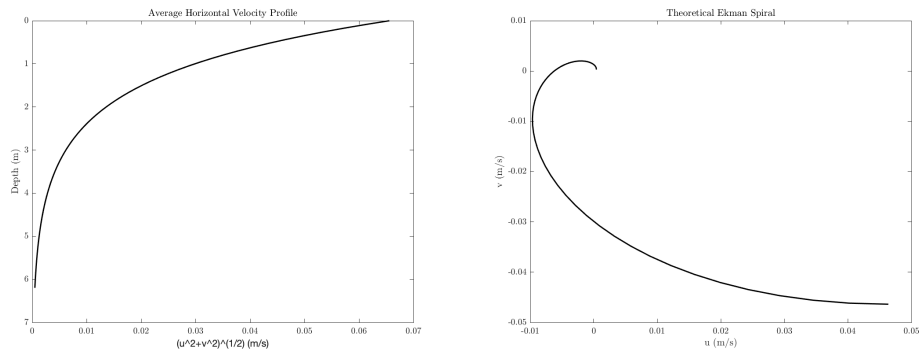


Figure 4.2: Mean horizontal velocity (u & v shown in figure (4.1) (left), and the associated Ekman spiral (right)

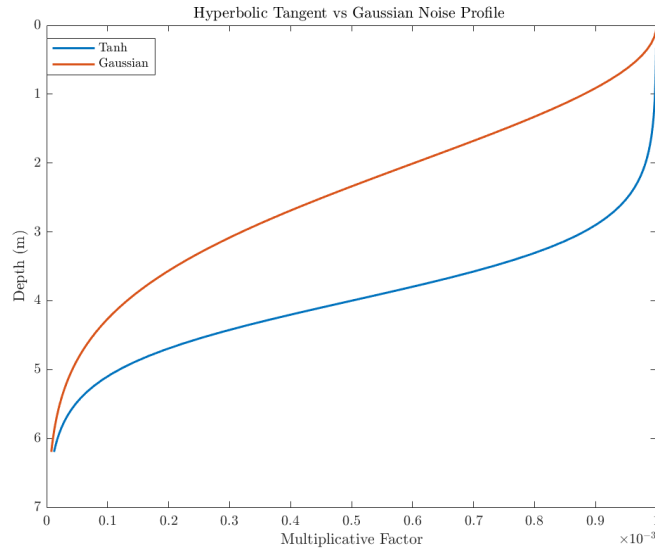


Figure 4.3: Half Gaussian versus hyperbolic tangent multiplicative factors as a function of depth.

4.2 FLUCTUATION FIELD

The initial perturbation field is initially conducted to be white noise, i.e. by random values varying from -1 to 1 . Moreover, this noise field is statistically homogeneous in xy - plane. Additional details on the construction of the turbulent fluctuations field is given in section (3.5). After creating the initial field, we then scale these velocity perturbations in a way that they have velocities less than 10% of the mean profile magnitude, everywhere throughout the domain. In an attempt to spatially focus the fluctuations in the vertical scale that higher velocity magnitudes are located in the upper layer, where the higher values of the mean profile are found, we experimented multiplying with two different windowing functions. Figure (4.3) shows these two windowing functions. The orange line represents a half Gaussian curve, where the peak of the curve lies on the surface of the domain. For the blue line, we made use of a hyperbolic tangent function. Both factors vary from 0 to 1 (multiplied by 10^{-3} in order to get the appropriate velocity magnitude). Their main difference, as shown, is that the "tanh" provides half of the domain with more than 90% of the higher absolute values. After testing both approaches, we concluded that the hyperbolic tangent serves better than the half Gaussian, as the latter produces a weaker perturbations' field. We finally add the perturbations field onto the mean velocity field. In figure (4.4), there is an example of a vertical profile for each velocity component.

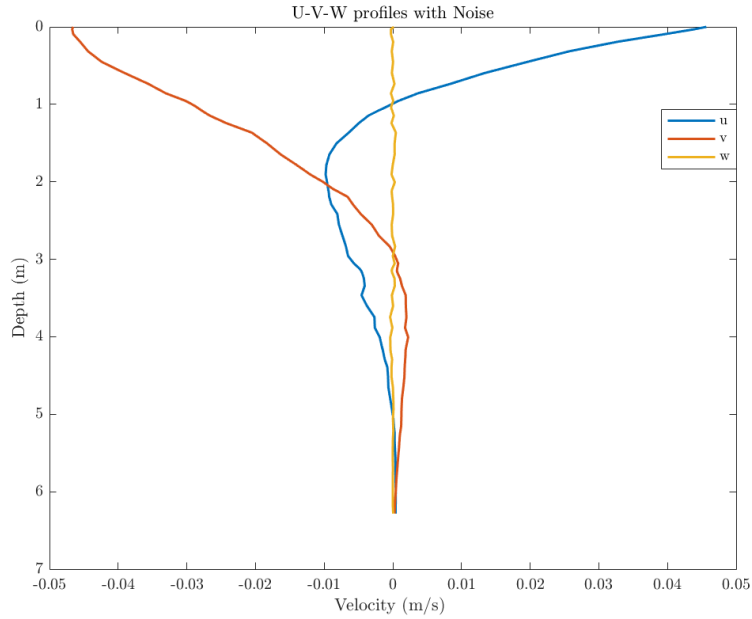


Figure 4.4: 1-D Initial vertical profiles of instantaneous background and perturbations sampled at $x=y=L/2$.

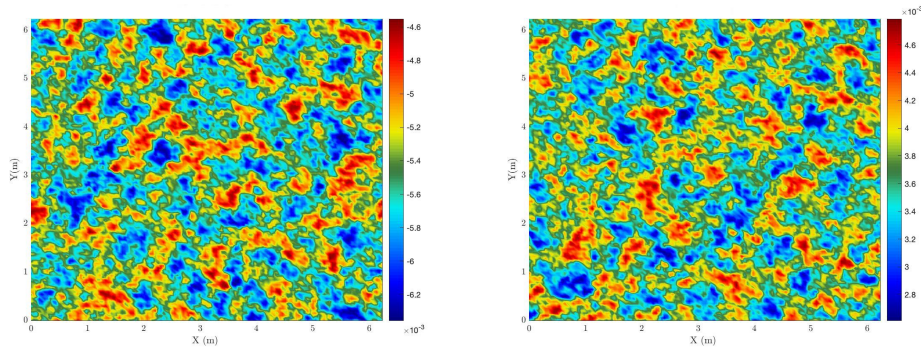


Figure 4.5: u contours in xy - plane in $z = L/2$ (left), and, in $z = L/8$ (right). We observe a similar pattern without direction preference. Colorbar limits are: $[-6.2, -4.6] \cdot 10^{-3}$ (left), $[2.8, 4.6] \cdot 10^{-3}$ (right)

Finally, the velocity field used for the initialization of the simulations is shown via contour plots on horizontal and vertical planes (figures 4.5, 4.6, 4.7). As expected, each component's xy plane structure follows a similar random pattern. In other words, the perturbations do not show any directional preference or adaptation to the mean profile, in the initial condition. This behavior is highlighted in figure (4.5), where u contours in the xy - plane are shown in two different depths.

In addition, taking advantage of the xy uniform structure of the mean profile, whose velocity values are $O(10)$ larger than those of the perturbations, we are able to compute a mean profile for the whole domain at any specific time. This calculation will be very useful, in order to subtract the perturbation field from the total one, in any time step needed. Moreover, in the initial state, there are not significant differences between $xz - plane$ and $yz - plane$ contour plots, as the pattern is dominated by the mean profile.

In figure (4.6), both u and v total, and corresponding perturbations contours are presented. As one may expect from the fact that we considered wind stress applied only in the x direction, the u component is characterized by a more intense gradient than the v component. In figure (4.7), w velocity contours both in the $xy - plane$ and in the $yz - plane$ are shown. It is obvious that the total w velocity field is reflected to perturbations, as confirmed by the equations (4.1) & (4.2).

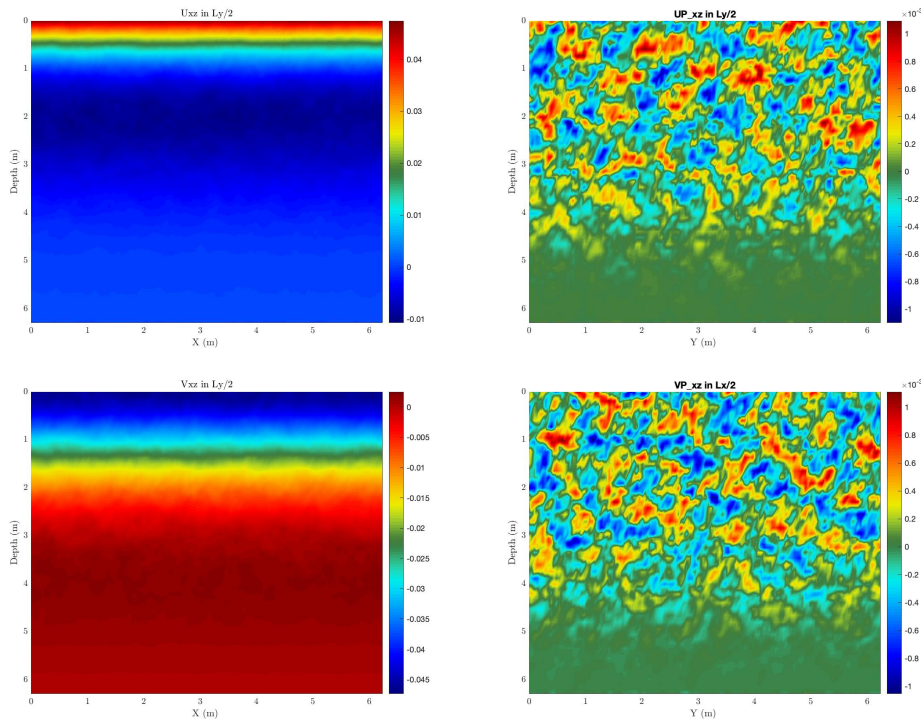


Figure 4.6: u_{total} and $u_{perturbation}$ velocity contours in the $xz - plane$ (top)
 v_{total} and $v_{perturbation}$ velocity contours in the $yz - plane$ (bottom)
 Colorbar limits are: $[-0.01, 0.05]$ (top-left), $[-0.05, 0.01]$ (bottom-left),
 $[-1, 1] \cdot 10^{-3}$ (right)

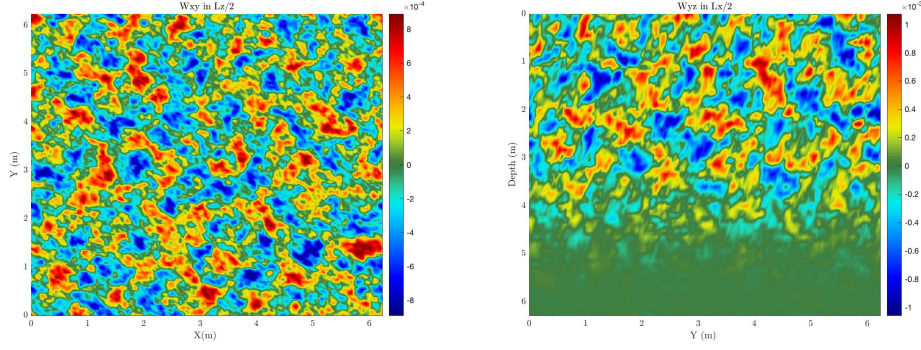


Figure 4.7: w contours in xy -plane(left), and in yz -plane(right).
Colorbar: $[-8,8] \cdot 10^{-4}$ (left), $[-1,1] \cdot 10^{-3}$ (right)

4.3 RELAXATION PROCEDURE

In the previous sections, we defined the initial state for the velocity, which will be used in our simulations. Before proceeding to the main unstratified run, one preliminary simulation takes place, the relaxation part. As discussed in detail in section (3.5) (see also figure 3.6), a relaxation procedure is introduced to correlate the fluctuations field with the mean velocity field, before the main calculation is performed. Although, this procedure is deemed as necessary in the simulation of wakes to avoid any rapid decay of the perturbations, described by Dommermuth et al., 2002, and, Diamessis et al., 2011, we are not completely confident that this procedure is necessary for the simulation of our Ekman layer. Nonetheless, following the procedure used in numerical wakes experiments, we will explore this preliminary run. In our case, we conducted two test runs for a short time period after initialization, in order to examine for any differences between using or not using the relaxation. For this purpose, we calculated the volume integral of the perturbation kinetic energy of the whole domain, for each run ($KE_{Pdomain} = \iiint KE_{pert} dx dy dz$). We then nondimensionalized this integral with the volume integral of the kinetic energy value of the initial state. Both the simulations are unstratified, where the density remains constant and the gradient is zero over the full domain depth ($\rho = \rho_0 = 1026 \text{ kg/m}^3$). The results are shown in figure (4.8).

The total duration of the relaxation process is a very important factor for the efficiency of this procedure. In order to ensure an appropriate duration, we are in need of finding a characteristic time scale of the phenomenon. For this purpose, we define a turnover time (T_t), based on a characteristic background velocity and Ekman depth (shown in equation 4.3). The total relaxation time should correspond to enough turnover times. We compute $T_t = 59.7 \text{ sec}$, while we run relaxation for 300 seconds of physical time. As a result, the corresponding total relaxation time is $R_{time} \simeq 5.03$ turnover times.

$$T_t = \frac{D}{|U_{max}|} \quad , \quad \text{where} \quad |U_{max}| = \sqrt{|u|^2 + |v|^2} \quad (4.3)$$

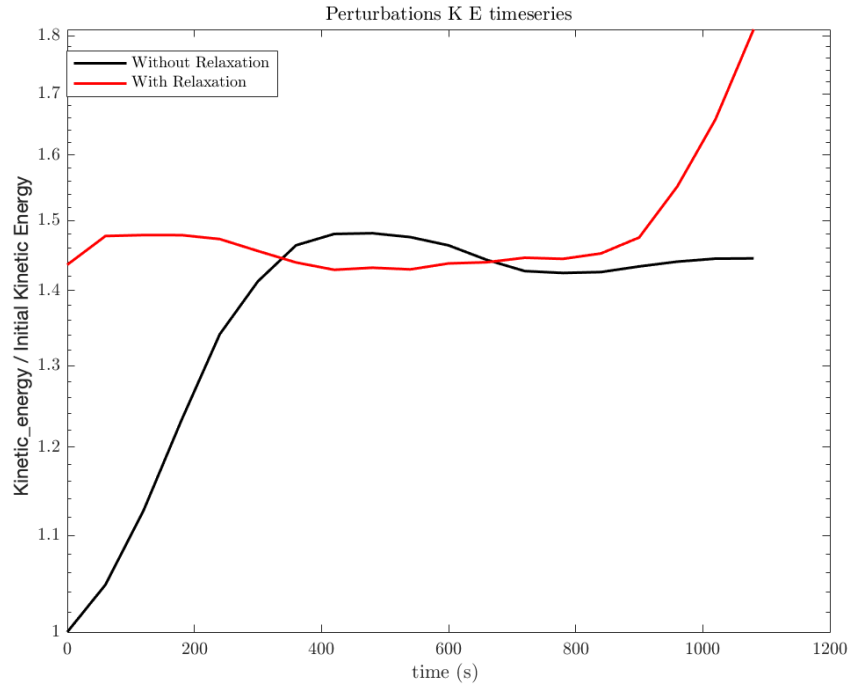


Figure 4.8: Kinetic Energy for two unstratified runs of 20 minutes each, with (red line) and without (black line) relaxation procedure

In figure (4.8), the red line begins after the relaxation run, while the black line does not include this procedure at all. We can observe that the case that included relaxation tends to increase the perturbations' kinetic energy after almost 14 minutes. However, we did not test the above behavior in a long run. Moreover, we did not have the time insist to on more tests and find the most satisfactory duration of the relaxation for our experiment. In any case, we will include the same relaxation of the above test in all following simulations, and the results will be shown after the relaxation period.

4.4 UNSTRATIFIED RESULTS

4.4.1 Flow visualization

In this section, we are going to present the main results of the unstratified case, initialized with the relaxation velocity field described above. The duration of the total actual production, post relaxation, is 40 minutes.

In figure (4.9), contours of the perturbations field of the u velocity in a $xy - plane$ after 40 minutes of simulation, are shown at 4 different depths. These plots show that the velocity perturbations feel the effect of the mean profile, in contrast with the initial state (figure 4.5).

Inspecting at figure (4.9), one could easily recognize that the pattern of the perturbations shows different orientations. This is happening due to the different directions of the mean horizontal velocity vector, to which the per-

turbations field has adapted. Additionally, the higher the position in the domain, where larger mean velocity values occur, the larger and more diffuse the contour patterns seem to be. At this point, it is essential to clarify that the total u on the $xy - plane$ appears to have the exact same pattern with the fluctuations field, multiplied by the mean horizontal velocity magnitude, in any z . Overall, we have established confidence that the code produces physically consistent vector after our initial set-up.

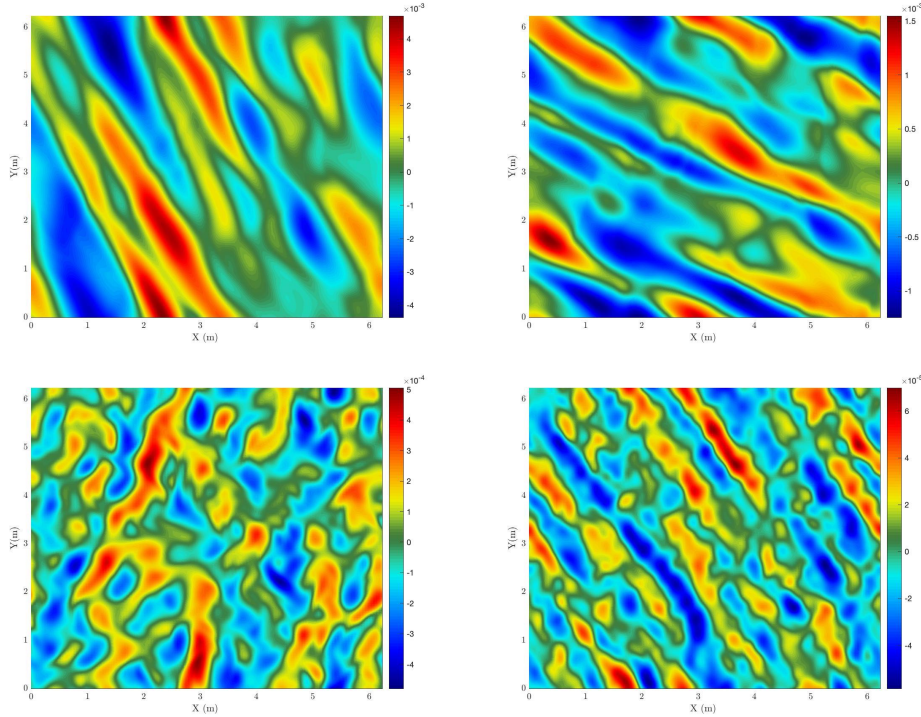


Figure 4.9: u perturbations in 4 different corresponding depths. Obvious direction preference is shown, compared to initial state (figure 4.5). Top-left $z=0.79\text{m}$, Top-right $z=1.57\text{m}$, Bottom-left $z=3.14\text{m}$, Bottom-right $z=5.24\text{m}$. Colorbar limits are: $[-4, 4] \cdot 10^{-3}$ (Top-left), $[-1.5, 1.5] \cdot 10^{-3}$ (Top-right), $[-5, 5] \cdot 10^{-4}$ (bottom-left), $[-6, 6] \cdot 10^{-5}$ (bottom-right)

In the following figures, the evolution of the structure of the velocity field will be presented. In figure (4.10), snapshots of the $xy - plane$ contours of u and v components, for two different time steps ($t_1 = 600\text{s}$ and $t_2 = 2400\text{s}$), are shown. The y coordinate of this transect is in the middle of the domain length. On $xz - plane$ (figure 4.10), the small-scale disturbances of the initial condition (figure 4.6) seem to eventually disappear, while larger-scale structures with wave-like characteristics take their place, located in the depth that the velocity gradient is larger for each component. In figure (4.11), we visualize the $xy - plane$ contours for both u and v . The vertical coordinate of this transect is equal to 2m , where $u_{mean} \simeq v_{mean}$, while the time chosen is the same with the above (t_1 and t_2). Looking at the results qualitatively, it is obvious that the structures appear more diffused and are characterized by larger spatial scales over time.

Subsequently, we will present contours of the w velocity. In figure (4.12), the $xy - plane$ contours are shown, for 3 different timesteps, at 2 different depths. Furthermore, in figure (4.13), we may see both xz and yz planes, where the third corresponding coordinate is located in the middle of the domain in each plot. The upper snapshots show the $xz - plane$, while the lower placed refer to the $yz - plane$. For all w' figures, snapshots on the left refer to 600s, while in the middle to 1200s, and on the right to 2400s, respectively. In figure (4.13), we can observe that the higher w values shift towards the surface over time. This evolution implies that, as time passes by, the initial small-scale w perturbations are concentrated in the upper layer, creating larger-scale structures. As a result, the vertical movements possibly would localize in the upper domain, keeping the rest of it almost still. In addition, the maximum w value is growing by almost one order of magnitude, after 40 simulated minutes.

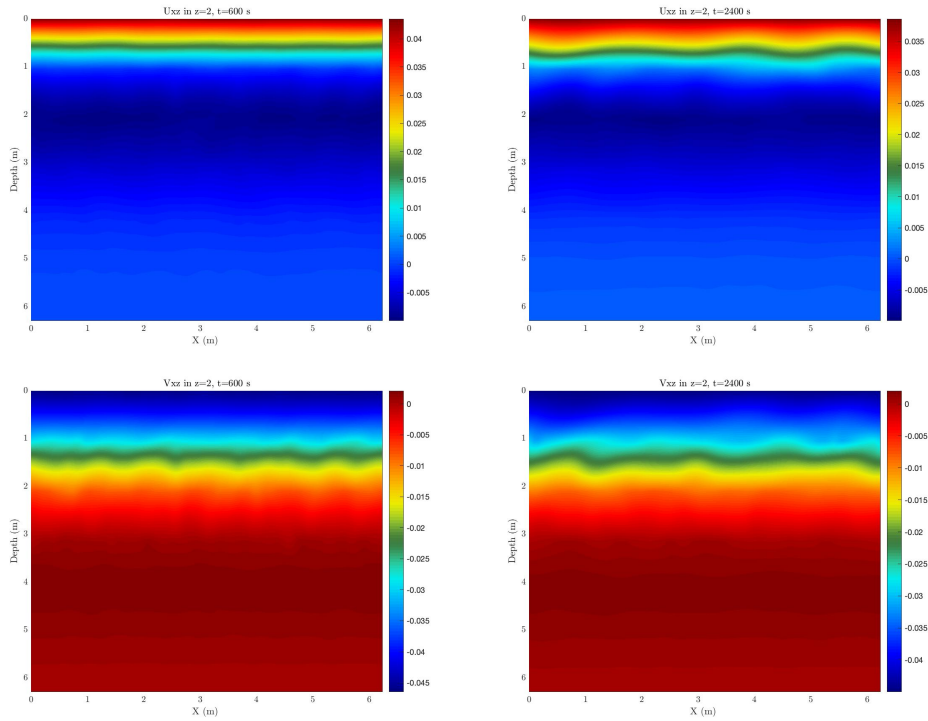


Figure 4.10: Contours of u in $xz - plane$ (top) and v in $xz - plane$ (bottom) in $y = \pi$ m. Left figures correspond to $t_1 = 600$ s, right figures to $t_2 = 2400$ s. Colorbar min & max are: $[-0.005, 0.04]$ (top), $[-0.045, 0.005]$ (bottom)

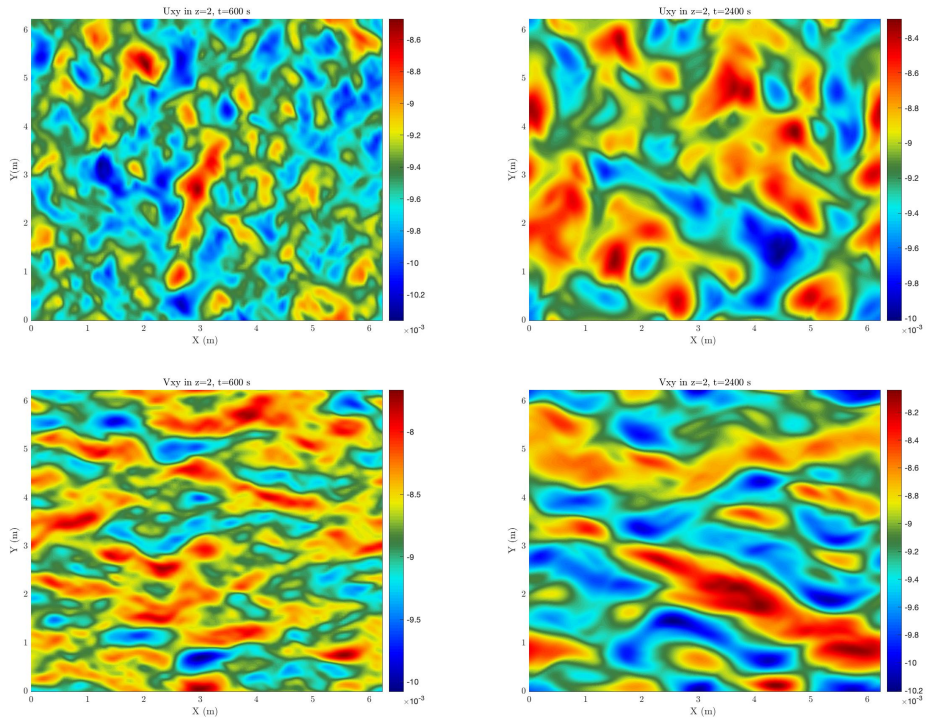


Figure 4.11: Contours of u (top) & v (bottom) (xy -plane, $z=2m$).
 $t_1=600s$ (left), $t_2=2400s$ (right) Colorbar limits are: $[-1,1] \cdot 10^{-2}$

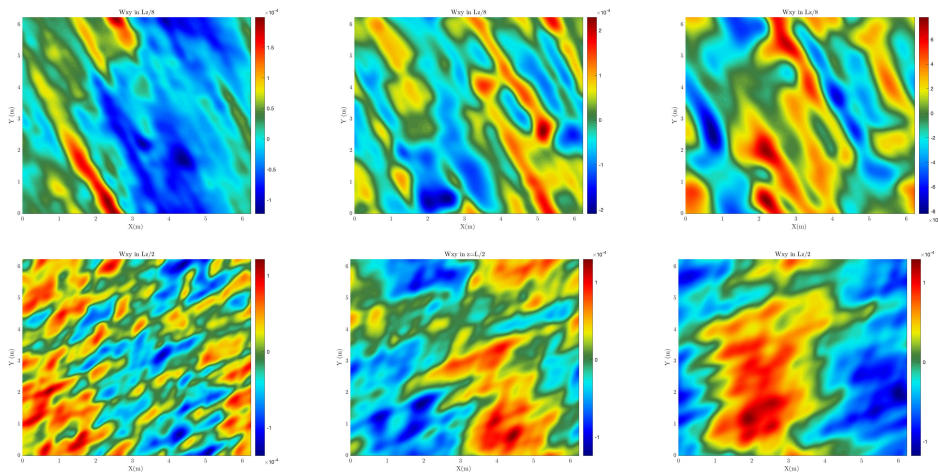


Figure 4.12: W contours in xy -plane ($z=0.79m$ (top), $z=7m$ (bottom)).
 Colorbar limits are $[-2,2]10^{-4}$ everywhere except from (top-right),
 where min & max are: $[-8,8]10^{-4}$

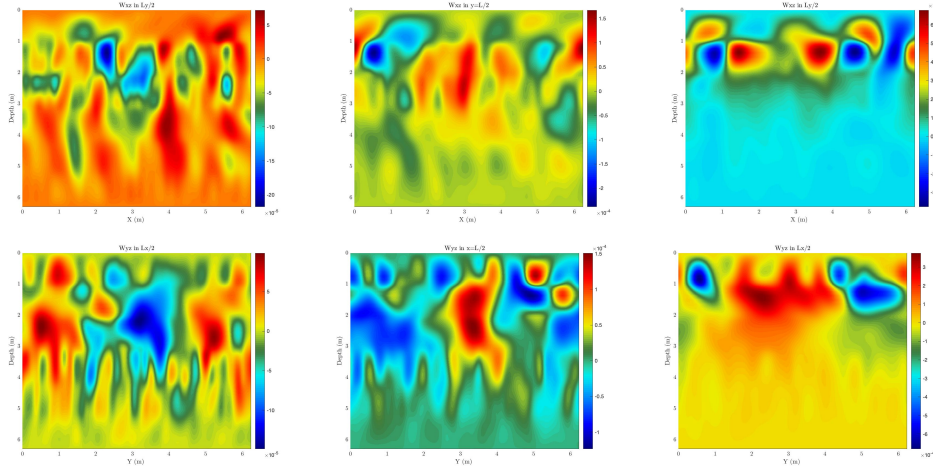


Figure 4.13: Contours of W in xz -plane (top), in yz -plane (bottom).
 Colorbar limits are: $[-20, 10] \cdot 10^{-5}$ (left), $[-2, 1.5] \cdot 10^{-4}$ (middle), $[-6, 6] \cdot 10^{-4}$ (right).

Similar behavior with the velocity perturbations' evolution over time is also found in the vorticity flow structure. Small-scaled disturbances develop in larger-in-length structures. To be more specific, in figure (4.14), the z -vorticity is shown (in a xy - plane) in the same 3 timesteps presented in figure (4.12). Moreover, the visualization of the vorticity is captured at two different depths, associated with one smaller and one larger mean horizontal velocity value, respectively. As expected, larger structures are found in the area driven by larger mean velocity. A remarkable observation is that in the lower layer ($z=\pi$ m), the structures seem more diffused and their maximum absolute value decreases over time. In the upper area ($z=1.57$ m), although the patterns seem to follow the same diffusive behavior, the maximum absolute vorticity value remains in the same order of magnitude.

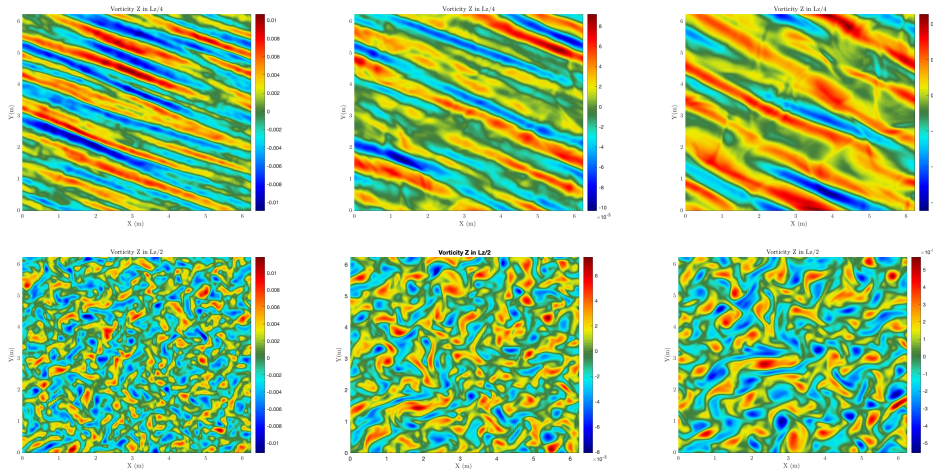


Figure 4.14: Z -vorticity for $z=1.57$ (top), $z = \pi$ (bottom). Colorbar limits are: $[-1, 1] \cdot 10^{-2}$ (top), $[-1, 1] \cdot 10^{-2}$ (bottom-left), $[-5, 5] \cdot 10^{-3}$ (bottom-right)

4.4.2 Quantitative results

Having now followed the development of the velocity field qualitatively, we will proceed to quantitatively monitor the kinetic energy of the flow. Assuming that the total velocity is the sum of the mean and the fluctuation field of all 3 components (more details in section 3.5, equations 3.12 - 3.13 - 3.14), the total velocity will be:

$$\overrightarrow{U_{total}} = u \cdot \hat{i} + v \cdot \hat{j} + w \cdot \hat{k} \Rightarrow |U_{total}|^2 = U_{mean}^2 + U_{pert}^2 + U_{mp}^2 \quad (4.4)$$

$$\text{where, } U_{mean}^2 = u_{mean}^2 + v_{mean}^2, \quad (4.5)$$

$$U_{pert}^2 = u'^2 + v'^2 + w'^2, \quad (4.6)$$

$$U_{mp}^2 = 2(u_{mean}u' + v_{mean}v') \quad (4.7)$$

The total kinetic energy per unit mass will be:

$$KE_i = \frac{KE_{total}(i)}{\rho} = \frac{|U_{total}|(i)^2}{2} \Rightarrow KE_i = KE_{mean}(i) + KE_{pert}(i) + KE_{mp}(i), \quad (4.8)$$

where we consider $i = i(x, y, z)$ as the index of any random position in our domain (i represents any combination of x, y and z). Therefore, the total kinetic energy of the whole domain will be the volume integral of the KE_i as:

$$KE = \iiint KE_i dx dy dz \quad (4.9)$$

We subsequently compute the mean kinetic energy value as well as the perturbations' kinetic energy. The KE_{mp} value lies in the order of 10^{-10} , and as a result we are justified in overlooking it in our calculations. In figure (4.15), we show the evolution in time of the total kinetic energy in the domain, for both the mean and perturbations, respectively. It is clear that the mean profile dominates the total kinetic energy behavior. Furthermore, we observe that the perturbations' kinetic energy is 3 orders of magnitude smaller than that of the mean profile. As a consequence, although the perturbations' kinetic energy rises over time, this rise is too small to impact the mean profile.

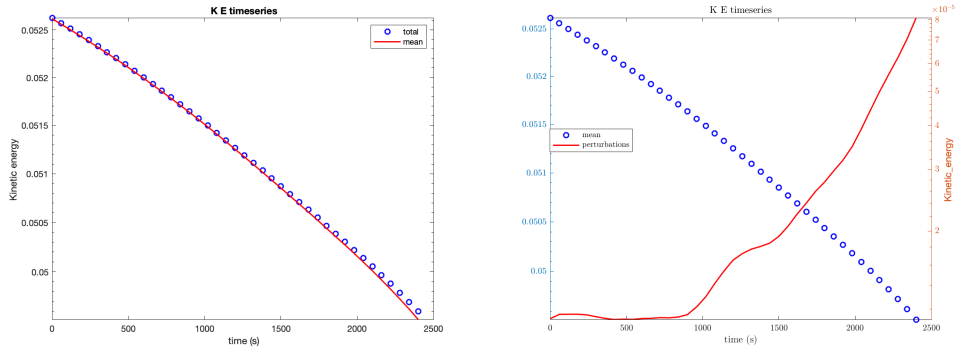


Figure 4.15: Total & mean kinetic energy (left), Mean & perturbations kinetic energy (right)

Finally, we compute the spatial spectrum of the kinetic energy in both horizontal directions, for different times and depths. In figure (4.16), the spatial spectrum of the kinetic energy as a function of wavenumber, in the x direction ($KE(Kx) = (|\hat{u}(Kx)|^2 + |\hat{v}(Kx)|^2)/2$), is shown, while in (4.17) it is presented in the y direction. In both figures, the blue line corresponds to a depth equal to 0.63m, while the red line to π m. The temporal evolution is monitored through 4 different times: $t = 0s$ $t = 600s$ $t = 1200s$ $t = 2400s$ from left to right.

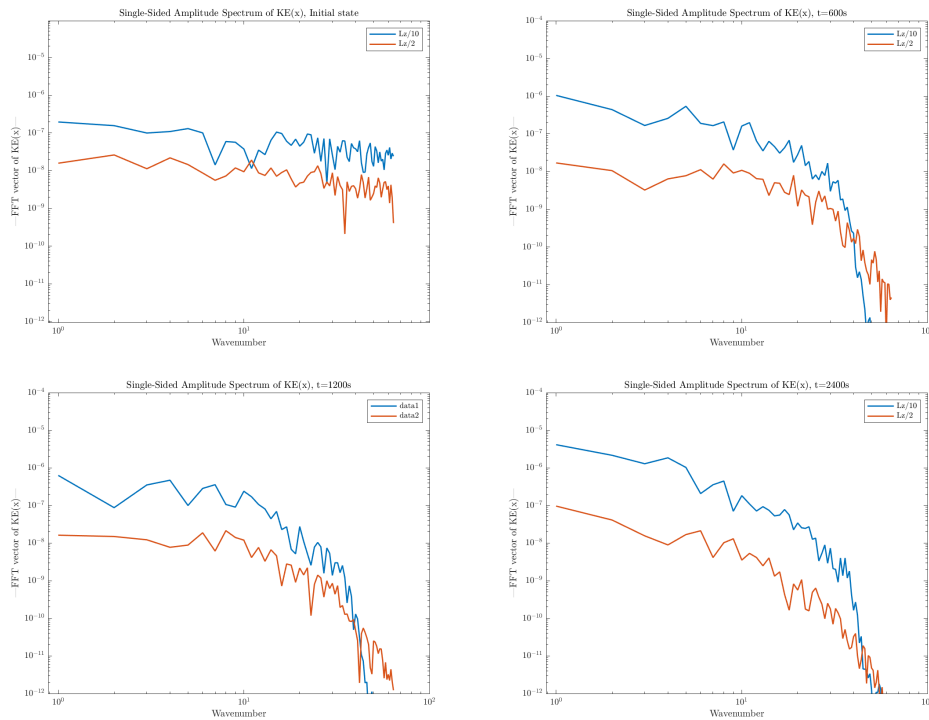


Figure 4.16: Total kinetic energy spectrum in x -direction. $t=0s$ (top-left), $t=600s$ (top-right), $t=1200s$ (bottom-left), $t=2400s$ (bottom-right)

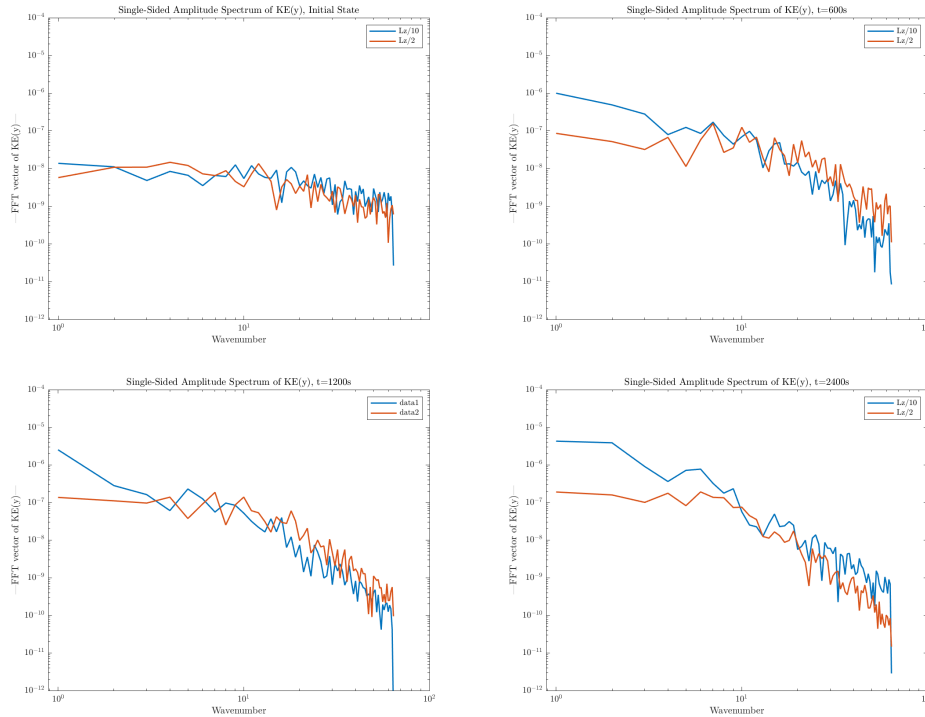


Figure 4.17: Total kinetic energy spectrum in y-direction. $t=0s$ (top-left), $t=600s$ (top-right), $t=1200s$ (bottom-left), $t=2400s$ (bottom-right)

4.5 STRATIFIED RESULTS

Whereas the previous section is used to monitor the behavior of the code initialized only by our complex velocity field, in this section we add a background density profile. We choose to begin with setting up a case with an idealized linear density gradient. The total density ρ (for details see section (3.1), equation (3.6)) as a function of depth, is shown in the left side of the figure (4.18). The Brunt-Vaisala frequency that corresponds to this profile, is, as expected, constant and equal to $N = 0.012 \text{ rad/s}$. In the right side of the same figure, the Richardson number is presented as a function of z , in logarithmic axis. This non-dimensional parameter has been calculated using the vertical shear produced by the horizontal mean velocity, shown in figure (4.2). As mentioned in section (2.1), it is necessary to reach a Ri less than $\frac{1}{4}$, for turbulence to develop and be maintained for some time. The red line highlights this critical value, and, what is more, it gives us an approximation of the vertical area where turbulence could develop. In a more realistic flow, the density profile shows complexity that results in a Ri that does not necessarily increase over depth. As a consequence, the fact that the turbulent area coincides with the upper layer of the domain, is a result of the idealized assumptions of this case.

The duration of the stratified run is the same as the unstratified one (total time = 40minutes). In the following figures, the evolution of the velocity

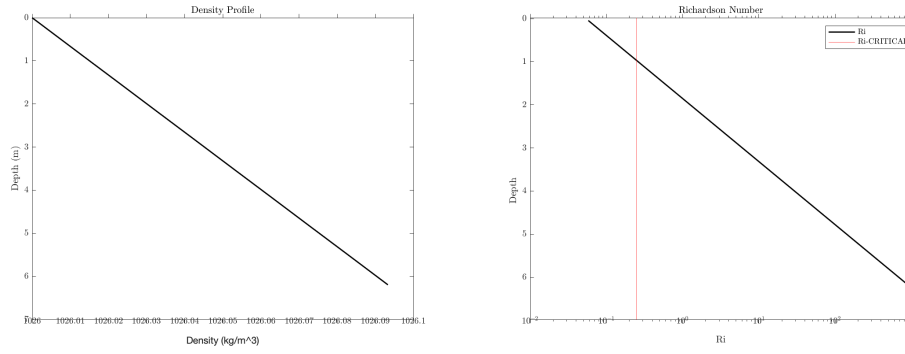


Figure 4.18: (left) Density profile, x-axis limits are:[1026,1026.1]
 (right) Richardson number logarithmic profile, x-axis limits are:[$10^{-2}, 10^3$]

fields will be provided at 3 different times ($t_1 = 600s$, $t_2 = 1200s$, and $t_3 = 2400s$). In figure (4.19), the evolution of w contours in both $xz - plane$ and $yz - plane$ is shown, at the above mentioned times. The behavior appears similar to the corresponding of the unstratified case visualization. In figures (4.20), (4.21) and (4.22), the evolution of each velocity component on the $xy - plane$ is provided. The snapshots are taken at two different depths ($z_1 = L/10 m$ and $z_2 = L/2 m$), where z_1 refers to the area characterized by $Ri_{initial} < Ri_{critical}$, while z_2 to a $Ri_{initial} > Ri_{critical}$. Moreover, in figure (4.23) the z-vorticity contours are shown. The patterns do not show any significant difference, compared to the corresponding visualization of the unstratified case. However, regarding the upper layer in t_3 , the maximum value is smaller by one order of magnitude compared to the corresponding of the unstratified case.

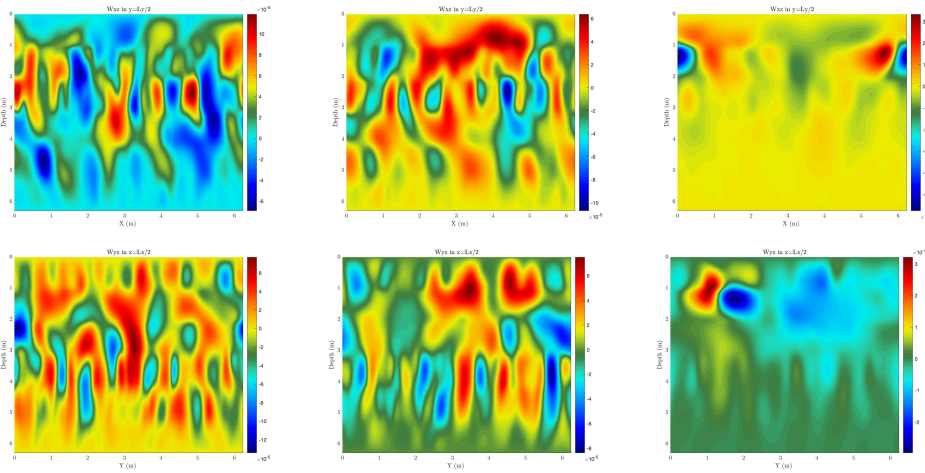


Figure 4.19: Contours of W in xz -plane (top), in yz -plane (bottom).
 Colorbar limits are: $[-1, 1] \cdot 10^{-4}$ to $[-3, 3] \cdot 10^{-4}$ (left to right).

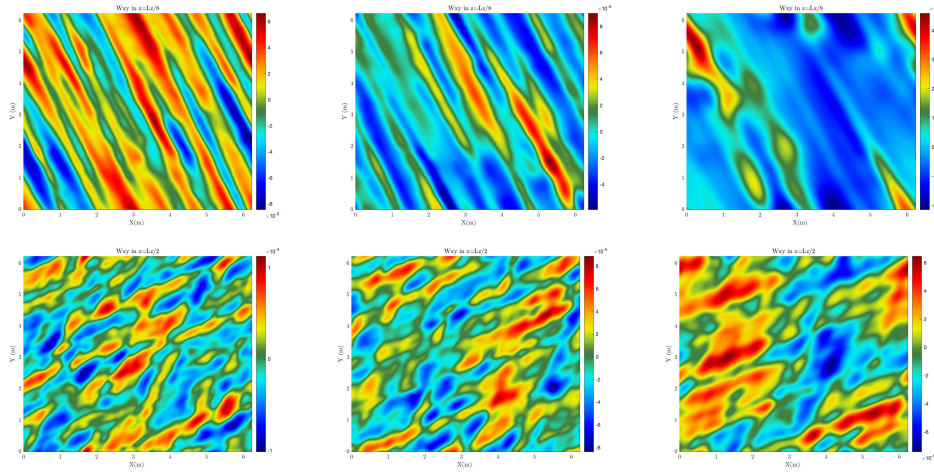


Figure 4.20: W contours in xy -plane ($z=L/10m$ (top), $z=L/2m$ (bottom)).
 Colorbar limits are: $[-8, 6] \cdot 10^{-5}$ to $[-2, 4] \cdot 10^{-4}$ (top - left to right),
 $[-1, 1] \cdot 10^{-4}$ to $[-6, 6] \cdot 10^{-5}$ (bottom - left to right)

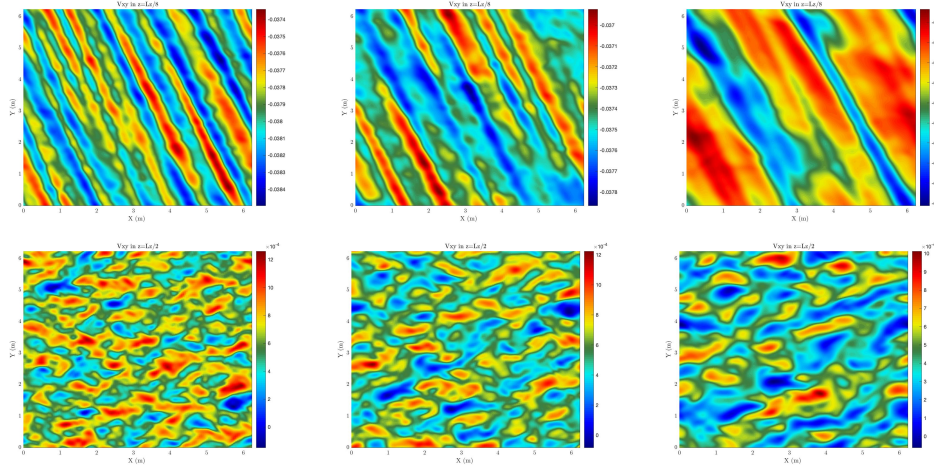


Figure 4.21: V contours in xy -plane ($z=L/10m$ (top), $z=L/2m$ (bottom)).
 Colorbar limits are: $[-0.0375, -0.0385]$ (top - left to right), $[0, 12] \cdot 10^{-4}$
 (bottom - left to right)

The velocity field interacts with and impacts the density field. As shown in equation (3.6), the total density constitutes the sum of 3, independent of each other, contributions. The first variable (ρ_0) is constant everywhere in the domain while the second one ($\bar{\rho}$) uses a constant gradient through the z -axis, and, what is more, $\bar{\rho}$ is kept frozen in every timestep. The final part (ρ') is set to zero in the initial state, while it remains free to vary during the simulation.

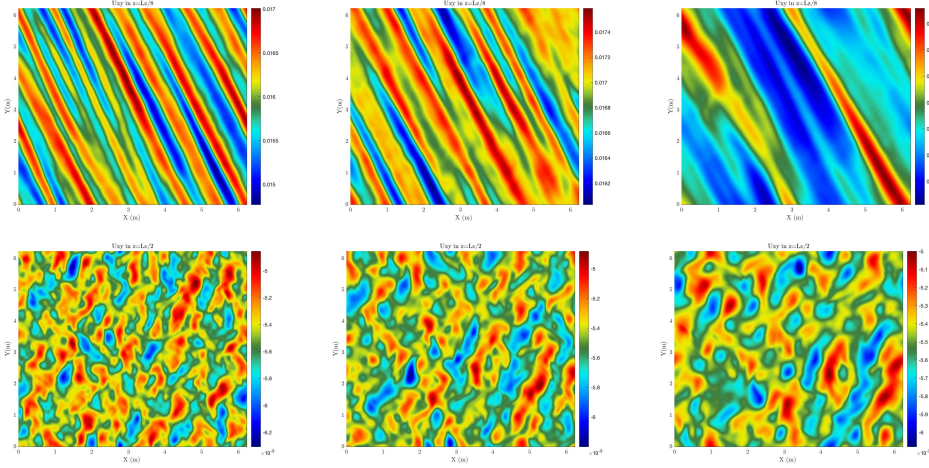


Figure 4.22: U contours in xy -plane ($z=L/10m$ (top), $z=L/2m$ (bottom)).
 Colorbar limits are: $[-0.02, -0.015]$ (top), $[-7, -5] \cdot 10^{-3}$ (bottom)

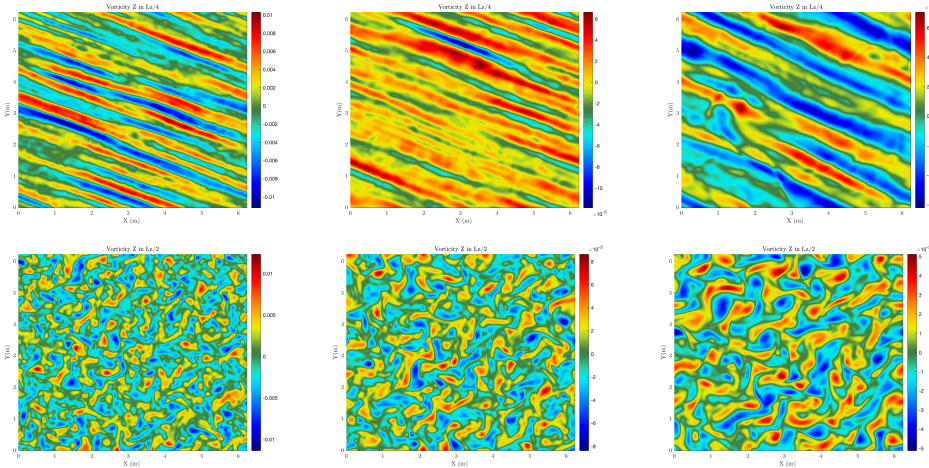


Figure 4.23: Z-vorticity contours in xy -plane ($z=L/4$ (top), $z=L/2$ (bottom)).
 Colorbar limits are: $[-1, 1] \cdot 10^{-2}$ (top), $[-1, 1] \cdot 10^{-2}$ to $[-5, 5] \cdot 10^{-3}$ (bottom - left to right)

In figure (4.24), the ρ' in xz - plane and in yz - plane is shown for the same t_1, t_2 and t_3 as above. In figure (4.25), we see the xy - plane of the density perturbation. These snapshots also refer to the same 2 different depths (z_1 and z_2) mentioned above. Although this needs further analysis, the evolution over time seems like there is a domain scale internal wave of varying mean amplitude that creates these weak highs and lows. It is important to highlight that we do not have enough data in the window $[0, 2\pi]$ to examine initial adjustment of turbulence to buoyancy.

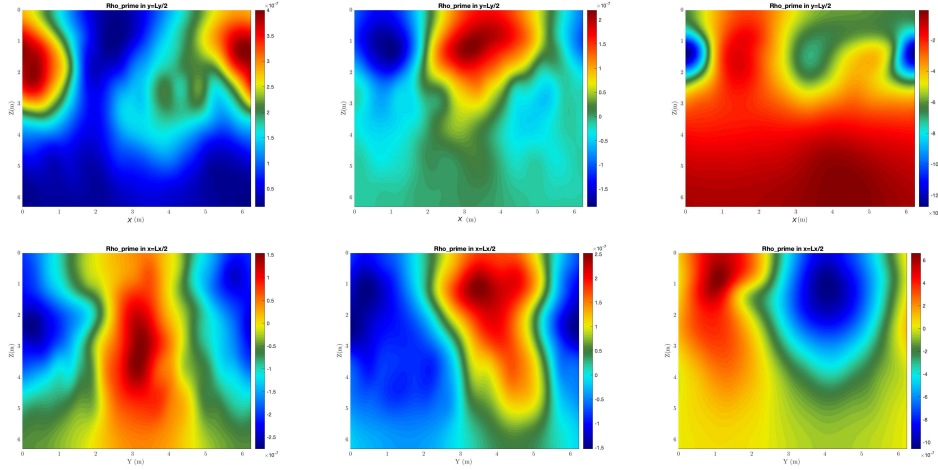


Figure 4.24: ρ' in xz -plane (top), yz -plane (bottom).
 Colorbar limits are: $[0, 4] \cdot 10^{-7}$ to $[-12, 0] \cdot 10^{-6}$ (top - left to right),
 $[-2.5, 1.5] \cdot 10^{-7}$ to $[-10, 6] \cdot 10^{-7}$ (bottom - left to right)

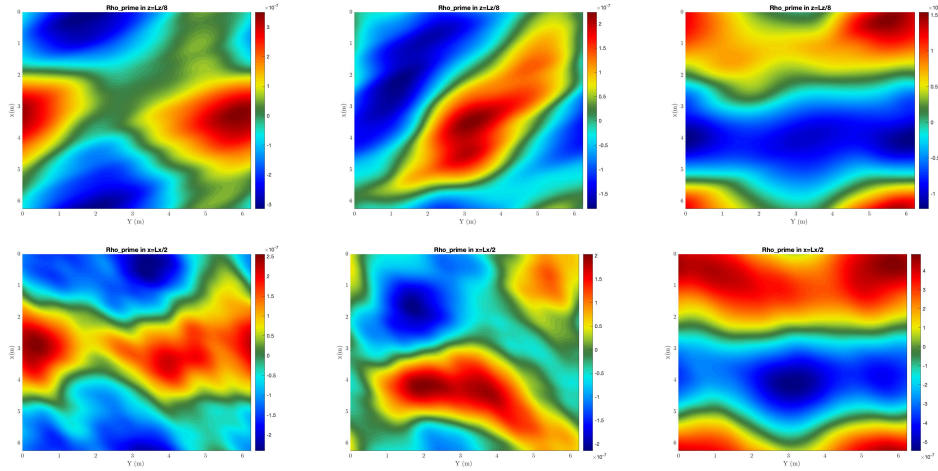


Figure 4.25: ρ' in xy -plane in $L/10$ (top), $L/2$ (bottom).
 Colorbar limits are: $[-3, 3] \cdot 10^{-7}$ to $[-1, 1] \cdot 10^{-6}$ (top - left to right),
 $[-2, 2] \cdot 10^{-7}$ to $[-5, 5] \cdot 10^{-7}$ (bottom - left to right)

Finally, in figure (4.26), the volume integral of kinetic energy of the mean profile, as well as the perturbations' kinetic energy, are shown and compared with the corresponding results of the unstratified case. Due to limited time and additional testing that is required, we cannot be confident the physical interpretation of those timeseries. More specifically, the fact that the curve of the kinetic energy of the mean profile in the stratified case is above the unstratified corresponding (figure 4.26 - left), remains a mystery. We could potentially attribute this difference to restratification effects, i.e. conversion of potential energy to kinetic energy as isopycnals return to their equilibrium position. Regarding the perturbations' kinetic energy, as expected their value is smaller during the whole simulation, probably due to the stratifica-

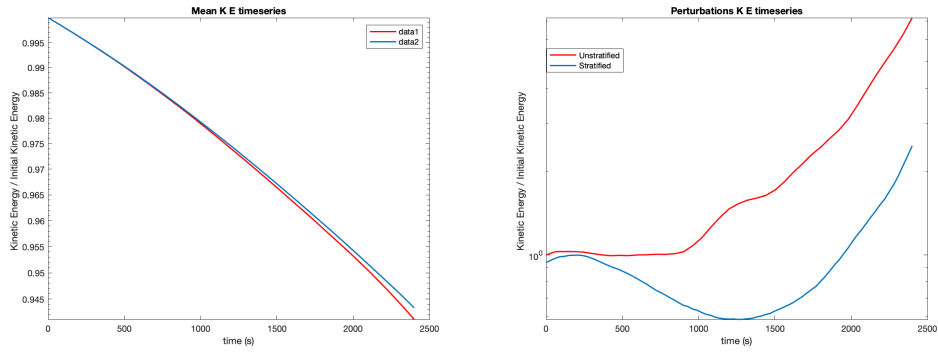


Figure 4.26: Mean-kinetic energy (left), Perturbations-kinetic energy (right). Comparison between unstratified (red line) and stratified case (blue line).

tion effect. However, we cannot determine the reason of the kinetic energy growth after 20 minutes of simulation.

In an attempt to explain this growth, the integral of the kinetic energy of the horizontal components, as well as for the vertical one, is shown in the figure (4.27). In this plot, we may observe that all 3 components are smaller than the corresponding of the unstratified case. Nonetheless, these results refer to the whole domain. Although we saw previously that w tends to concentrate in the upper layer, we did not have the time to calculate this energy per different vertical domain subsections.

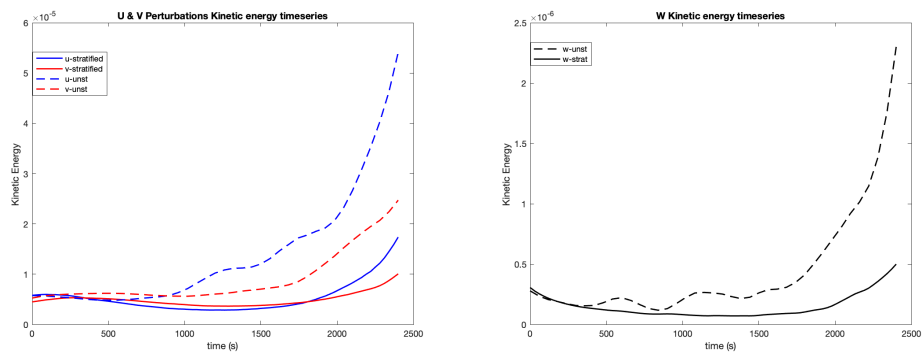


Figure 4.27: Horizontal K E perturbations (left), Vertical K E Perturbations(right). Comparison between unstratified (dashed line) and stratified case (solid line).

CONCLUSION AND DISCUSSION

5.1 SUMMARY & CONNECTION WITH PROJECT OBJECTIVES

This study has aimed to explore the development of turbulence in a stratified surface oceanic Ekman velocity field, through the use of spectral Implicit Large Eddy Simulations. Adopting the approach known as "bypass transition to turbulence", we construct the initial state of a theoretical Ekman-spiral-driven turbulent layer. Through the use of an incompressible spectral Fourier / modal-spectral-element-method solver, we localize our interest in the examination of turbulent events inside a spiral-shaped velocity profile, and, we analyze and compare the results of one unstratified and one stratified case. Both experiments were conducted at a predefined Reynolds number ($Re \sim 10^5$).

In summary, we constructed an initial state that included a mean Ekman velocity and a fluctuations' field. As for the latter, we created a non-uniform and statistically homogeneous fluctuations field in the $xy - plane$ and concluded that the most appropriate way of windowing it in the vertical direction is through the use of a multiplicative factor, based on a hyperbolic tangent function (compared to the half Gaussian profile). We then shortly tested the behavior of the code including a preliminary simulation, called "relaxation", and, subsequently used it in the simulations that followed.

In a 40-minute physical time simulation, that was generated after an almost 7-hours of computational time using 128 processors, we investigated an unstratified case. In this experiment, we observed the predefined perturbations' field correlate with the mean flow, and as a consequence, the $xy - plane$ pattern of the velocity components to appear more stretched in regions with larger shear. Moreover, we visualized the temporal evolution of the small-scale perturbations and observed that their pattern appeared more diffused and larger in length scale over time. Similar observations were made for the z-vorticity field. Finally, we followed by quantifying the total kinetic energy and its spatial spectrum in each horizontal direction. The integral of the domain's kinetic energy was calculated, both for the mean profile and for the perturbations. It was obvious that the mean profile's kinetic energy decays over time, possibly as an effect of viscosity, while the perturbations grow over time. However, this growth is 3 orders of magnitude smaller than the mean profile's value.

Regarding the stratified case, a 40-minute-long simulation was again conducted. All velocity parameters defined in the unstratified case were kept exactly the same, while a constant background density gradient was introduced. The associated Brunt-Vaisala frequency was selected in a way to secure a Richardson number less than its critical value in the upper region

of the domain. A qualitative analysis similar to the unstratified case was conducted. Furthermore, we visualized the density perturbations, where the patterns in all xy , xz , yz planes seem to imply the eventual establishment of a weak domain-scale internal wave. In addition, we compared the kinetic energy of the stratified experiment to the corresponding unstratified results. As expected, the perturbations' kinetic energy is decreased, compared to the associated behavior of the unstratified one. However, we did not have the time to divide the domain into vertical sub-regions in order to investigate thoroughly the stratified results as a function of depth. Hence, more research in this scientific project should be conducted in the future.

At this point, a discussion about our original goals is included. We started this study more ambitiously, aiming to use the results of a regional-scale RANS simulation as the initial state of our ILES simulation. However, it turned out that it was necessary to begin with a simpler, idealized case. Regarding the original project objectives, the chosen initial profiles are sampled from a 1D-NEMO configuration (Nucleus for European Modelling of the Ocean), built for the PAPA station in North Pacific and described in Reffray et al., 2015. NEMO is generally based on the 3-D primitive equations resulting from Reynolds averaging of the Navier–Stokes equations and transport equations for temperature and salinity. To focus on vertical turbulent mixing, we used NEMO-1D, a feature included in NEMO, to consider only one column of water. Although all the different closure schemes referred to in section (2.3) were used in different runs, the results selected were derived from the "k- ϵ " method. Our initial plan also included an analysis of the relationship between the turbulent flow field and the induced variation of the depth of the seasonal thermocline, inside the Ekman layer region. Last but not least, a preliminary calculation of the LES-calculated eddy diffusivity coefficients would complete the goals of this study. However, reality forced us to reconsider these goals. To be more specific, we had to deal with issues concerning the code setup, which, in conjunction with the limited-available time of a masters' thesis, led us to a more conservative study with more modest objectives. Although the results of the NEMO model mentioned above have been produced, we did not manage to use them as drivers in the LES as expected.

5.2 EXTRAPOLATING THE CURRENT DATA SET INTO THE OCEAN

Our computational domain described in section (3.3), in reality, effectively represents a tank-scale experiment, instead of a real oceanic region. As a result of the limited-available time of the masters' thesis and of some issues concerning the numerical stability of the code, which is being updated, we had to become more conservative in our research. Our initial goal was to simulate an oceanic region characterized by a cubic box with a length 10 to 20 times bigger than our actual current domain size. To extrapolate the current data set into real oceanic conditions, one needs to re-scale some of the main non-dimensional parameters.

First of all, the domain length would be 20 to 200 times larger, for a domain length equal to 120m to 1200m, respectively. As a consequence, the Reynolds number (see section 2.1) would be 10 to 1000 times larger than the currently defined Re , if one needs velocities up to 10 times larger. These scales are an example of the separation that exists between the real ocean and the computational laboratory simulations. It is obvious that one would need more than 1000 points in each direction (referring to 120m-based domain), in order to capture the various length scales at an appropriate resolution/accuracy.

Additionally, for the Richardson number (see section 2.1) to remain constant, in order to contain both turbulent and non-turbulent regions, one should either reduce the density gradient or increase the vertical velocity gradient. In our study, both the Brunt-Vaisala frequency and the velocity gradient values, are chosen in such a way that secures this transition to smaller or larger gradients, without escaping real observable oceanic conditions.

Last but not least, an area of interest more than 100 or 1000 times larger than the present domain length, considering the same to 10 times larger maximum velocity magnitude, would necessitate introduction of another term in the Navier-Stokes equations, the Coriolis force. This is clearly shown if one tries to re-calculate the Rossby number (see section 3.2). In conclusion, all of those re-scaling factors would practically mean more computational power in conjunction with computational time.

5.3 FUTURE WORK

Regarding the future work of this research project, there are many developments that one can pursue. To begin with, more tests on finding the most appropriate time for the relaxation procedure are necessary. As for the stratified case, more tests should be performed in the field of the mean kinetic energy and the associated smaller decrease over time, in contrast with the corresponding unstratified one. Moreover, one should turn the top boundary conditions for velocity to finite wind stress over the whole surface of the domain. Although this step is easy to incorporate in the code, we kept free-slip boundary conditions due to numerical instabilities that appeared and lack of time to deal with them. As far as the time-stepping scheme is concerned, there is an alternative option: an adaptive time-stepping scheme, which is employed to smoothly increase the time step during the less energetic buoyancy-dominated regime of the flow evolution, thereby minimizing the cost of advancing the simulations as far as possible in time. The adaptive time-stepping scheme is activated whenever the time step reaches the lower or upper bound of the vertical CFL criterion and the time step is increased or decreased. In addition, it is crucial for the oceanic research field to shift this research region to larger domain lengths/depths (as the scales referred to above). For a computational domain that represents at least a cubic box of $\sim 120m$ in length, the procedure described in section (5.2) must be carefully conducted. In these larger scales, one should calculate the characteristic turbulent length and time scales.

At this point, it is essential to highlight that there is more than one approach in the literature. More specifically, "Zikanov et al., 2003" define the Turbulent Length Scale (TLS) as shown in equation (5.1), while "Pham et al., 2017" compute the same variable as shown in equation (5.2). Both approaches use the friction velocity u_* shown in equation (5.3), where τ is the wind surface stress. This characteristic length scale is responsible for turbulent entrainment, so it needs to be well resolved in order to obtain an accurate entrainment law. Moreover, in "Pham et al., 2017", another important characteristic length scale is introduced: the buoyancy length scale (BLS) shown in equation (5.4). As the stratification increases among the cases, the scales of the turbulent motion get smaller in the same manner as the buoyancy length scale, as discussed in detail in "Pham et al., 2017". Regarding the time scales, the non-dimensional $N \cdot t$ is commonly used (N is the Brunt-Vaisala frequency). Nevertheless, the Eddy turnover time (E_t) is typically used, too (shown in equation 5.5). The added value of these characteristic scales is that gives the reader the opportunity to monitor the development of a turbulent event properly, and, as a result, to understand better any general characteristics of the motion. Furthermore, it is easier for one to investigate scale-dependent turbulent mixing processes in the surface Ekman layer by examining flow structure visualization.

$$TLS_Z = \frac{U_*}{f} \quad (5.1)$$

$$TLS_{PS} = \frac{U_*}{\sqrt{N \cdot f}} \quad (5.2)$$

$$U_* = \sqrt{\frac{\tau}{\rho_0}} \quad (5.3)$$

$$BLS_{PS} = \frac{U_*}{N} \quad (5.4)$$

$$E_t = \frac{L}{U} \quad (5.5)$$

Finally, alongside the transition to larger domain length, one should construct the initial state using the results of a RANS model or field observations. The most significant parameters that would be sampled from the large-scale model are the density profile and the mean velocity profile. The profiles shown in figure (5.1) are sampled from the NEMO 1D built for the PAPA station in North Pacific (referred to in section 5.1), where the latitude of the computed Coriolis is located (shown in figure 3.2). These profiles, in conjunction with the rest of the parameters that constitute the initial conditions, serve both of the following goals: At first, one can use the LES-calculated eddy diffusivity coefficients in order to enable an assessment of the effectiveness of large-scale model parameterization. In addition, it would be a pioneer study to use the results from a RANS model as the LES initial state, because, that would raise the opportunity for an easy and cheap way to find data sets to initialize LES models with less idealized assumptions and more realistic conditions.

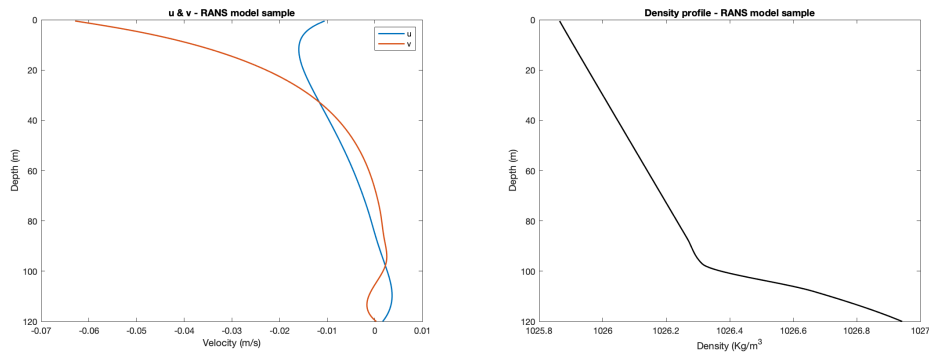


Figure 5.1: Velocity profiles (left), Density profile (right)
Both are sampled from RANS NEMO model

Part II

APPENDIX

BIBLIOGRAPHY

- Boris, J P, F F Grinstein, E S Oran, and R L Kolbe (1992). "New insights into large eddy simulation." In: *Fluid Dynamics Research* 10.4-6, pp. 199–228. ISSN: 0169-5983. DOI: [10.1016/0169-5983\(92\)90023-P](https://doi.org/10.1016/0169-5983(92)90023-P). URL: [https://iopscience.iop.org/article/10.1016/0169-5983\(92\)90023-P](https://iopscience.iop.org/article/10.1016/0169-5983(92)90023-P).
- Boyd, John Philip (1989). *Chebyshev & Fourier Spectral Methods*. Vol. 49. Lecture Notes in Engineering. Berlin, Heidelberg: Springer Berlin Heidelberg. ISBN: 978-3-540-51487-9. DOI: [10.1007/978-3-642-83876-7](https://doi.org/10.1007/978-3-642-83876-7). URL: <http://link.springer.com/10.1007/978-3-642-83876-7>.
- Clercx, H.J.H. and C.-H. Bruneau (2006). "The normal and oblique collision of a dipole with a no-slip boundary." In: *Computers & Fluids* 35.3, pp. 245–279. ISSN: 00457930. DOI: [10.1016/j.compfluid.2004.11.009](https://doi.org/10.1016/j.compfluid.2004.11.009). URL: <https://linkinghub.elsevier.com/retrieve/pii/S004579300500037X>.
- Cushman-Roisin, Benoit and Jean-Marie Beckers (2011). "The Ekman Layer." In: pp. 239–270. DOI: [10.1016/B978-0-12-088759-0.00008-0](https://doi.org/10.1016/B978-0-12-088759-0.00008-0). URL: <https://linkinghub.elsevier.com/retrieve/pii/B9780120887590000080>.
- Cuxart, J., P. Bougeault, and J.-L. Redelsperger (2000). "A turbulence scheme allowing for mesoscale and large-eddy simulations." In: *Quarterly Journal of the Royal Meteorological Society* 126.562, pp. 1–30. ISSN: 00359009. DOI: [10.1002/qj.49712656202](https://doi.org/10.1002/qj.49712656202). URL: <http://doi.wiley.com/10.1002/qj.49712656202>.
- Deleersnijder, Eric, Emmanuel Hanert, Hans Burchard, and Henk A. Dijkstra (2008). "On the mathematical stability of stratified flow models with local turbulence closure schemes." In: *Ocean Dynamics* 58.3-4, pp. 237–246. ISSN: 1616-7341. DOI: [10.1007/s10236-008-0145-6](https://doi.org/10.1007/s10236-008-0145-6). URL: <http://link.springer.com/10.1007/s10236-008-0145-6>.
- Diamassis, PETER J., GEOFFREY R. SPEDDING, and J. ANDRZEJ DOMARADZKI (2011). "Similarity scaling and vorticity structure in high-Reynolds-number stably stratified turbulent wakes." In: *Journal of Fluid Mechanics* 671, pp. 52–95. ISSN: 0022-1120. DOI: [10.1017/S0022112010005549](https://doi.org/10.1017/S0022112010005549). URL: https://www.cambridge.org/core/product/identifier/S0022112010005549/type/journal_article.
- Diamassis, P.J., J.A. Domaradzki, and J.S. Hesthaven (2005). "A spectral multidomain penalty method model for the simulation of high Reynolds number localized incompressible stratified turbulence." In: *Journal of Computational Physics* 202.1, pp. 298–322. ISSN: 00219991. DOI: [10.1016/j.jcp.2004.07.007](https://doi.org/10.1016/j.jcp.2004.07.007). URL: <https://linkinghub.elsevier.com/retrieve/pii/S0021999104002876>.
- Dommermuth, DOUGLAS G., JAMES W. ROTTMAN, GEORGE E. INNIS, and EVGENY A. NOVIKOV (2002). "Numerical simulation of the wake of a towed sphere in a weakly stratified fluid." In: *Journal of Fluid Mechanics* 473, pp. 83–101. ISSN: 0022-1120. DOI: [10.1017/S0022112002002276](https://doi.org/10.1017/S0022112002002276).

- URL: <https://www.cambridge.org/core/product/identifier/S0022112002002276/type/journal%7B%7Darticle>.
- Dunphy, M., C. Subich, and M. Stastna (2011). "Spectral methods for internal waves: indistinguishable density profiles and double-humped solitary waves." In: *Nonlinear Processes in Geophysics* 18.3, pp. 351–358. ISSN: 1607-7946. DOI: [10.5194/npg-18-351-2011](https://doi.org/10.5194/npg-18-351-2011). URL: <https://npg.copernicus.org/articles/18/351/2011/>.
- Durran, Dale R. (2010). *Numerical Methods for Fluid Dynamics*. Vol. 32. Texts in Applied Mathematics. New York, NY: Springer New York. ISBN: 978-1-4419-6411-3. DOI: [10.1007/978-1-4419-6412-0](https://doi.org/10.1007/978-1-4419-6412-0). URL: <http://link.springer.com/10.1007/978-1-4419-6412-0>.
- Ferziger, Joel H., Milovan Perić, and Robert L. Street (2020). *Computational Methods for Fluid Dynamics*. Cham: Springer International Publishing. ISBN: 978-3-319-99691-2. DOI: [10.1007/978-3-319-99693-6](https://doi.org/10.1007/978-3-319-99693-6). URL: <http://link.springer.com/10.1007/978-3-319-99693-6>.
- Fureby, Christer and Fernando F. Grinstein (2002). "Large Eddy Simulation of High-Reynolds-Number Free and Wall-Bounded Flows." In: *Journal of Computational Physics* 181.1, pp. 68–97. ISSN: 00219991. DOI: [10.1006/jcph.2002.7119](https://doi.org/10.1006/jcph.2002.7119). URL: <https://linkinghub.elsevier.com/retrieve/pii/S0021999102971196>.
- Hanjalić, K. (1994). "Advanced turbulence closure models: a view of current status and future prospects." In: *International Journal of Heat and Fluid Flow* 15.3, pp. 178–203. ISSN: 0142727X. DOI: [10.1016/0142-727X\(94\)90038-8](https://doi.org/10.1016/0142-727X(94)90038-8). URL: <https://linkinghub.elsevier.com/retrieve/pii/0142727X94900388>.
- Hesthaven, Jan S. and Tim Warburton (2008). *Nodal Discontinuous Galerkin Methods*. Vol. 54. Texts in Applied Mathematics. New York, NY: Springer New York. ISBN: 978-0-387-72065-4. DOI: [10.1007/978-0-387-72067-8](https://doi.org/10.1007/978-0-387-72067-8). URL: <http://link.springer.com/10.1007/978-0-387-72067-8>.
- Jacobs, R. G. and P. A. DURBIN (2001). "Simulations of bypass transition." In: *Journal of Fluid Mechanics* 428, pp. 185–212. ISSN: 0022-1120. DOI: [10.1017/S0022112000002469](https://doi.org/10.1017/S0022112000002469). URL: <https://www.cambridge.org/core/product/identifier/S0022112000002469/type/journal%7B%7Darticle>.
- Kato, H. and O. M. Phillips (1969). "On the penetration of a turbulent layer into stratified fluid." In: *Journal of Fluid Mechanics* 37.4, pp. 643–655. ISSN: 0022-1120. DOI: [10.1017/S0022112069000784](https://doi.org/10.1017/S0022112069000784). URL: <https://www.cambridge.org/core/product/identifier/S0022112069000784/type/journal%7B%7Darticle>.
- Kundu (2012). "Turbulence." In: *Fluid Mechanics*. Elsevier, pp. 541–620. DOI: [10.1016/B978-0-12-382100-3.10012-5](https://doi.org/10.1016/B978-0-12-382100-3.10012-5). URL: <https://linkinghub.elsevier.com/retrieve/pii/B9780123821003100125>.
- Large, W. G., J. C. McWilliams, and S. C. Doney (1994). "Oceanic vertical mixing: A review and a model with a nonlocal boundary layer parameterization." In: *Reviews of Geophysics* 32.4, p. 363. ISSN: 8755-1209. DOI: [10.1029/94RG01872](https://doi.org/10.1029/94RG01872). URL: <http://doi.wiley.com/10.1029/94RG01872>.

- Li, Qing et al. (2019). "Comparing Ocean Surface Boundary Vertical Mixing Schemes Including Langmuir Turbulence." In: *Journal of Advances in Modeling Earth Systems* 11.11, pp. 3545–3592. ISSN: 1942-2466. DOI: [10.1029/2019MS001810](https://doi.org/10.1029/2019MS001810). URL: <https://onlinelibrary.wiley.com/doi/abs/10.1029/2019MS001810>.
- Mellor, George L. and Tetsuji Yamada (1982). "Development of a turbulence closure model for geophysical fluid problems." In: *Reviews of Geophysics* 20.4, p. 851. ISSN: 8755-1209. DOI: [10.1029/RG020i004p00851](https://doi.org/10.1029/RG020i004p00851). URL: <http://doi.wiley.com/10.1029/RG020i004p00851>.
- Peters, H., M. C. Gregg, and J. M. Toole (1988). "On the parameterization of equatorial turbulence." In: *Journal of Geophysical Research* 93.C2, p. 1199. ISSN: 0148-0227. DOI: [10.1029/JC093iC02p01199](https://doi.org/10.1029/JC093iC02p01199). URL: <http://doi.wiley.com/10.1029/JC093iC02p01199>.
- Pham, H. T. and S. Sarkar (2017). "Turbulent entrainment in a strongly stratified barrier layer." In: *Journal of Geophysical Research: Oceans* 122.6, pp. 5075–5087. ISSN: 2169-9275. DOI: [10.1002/2016JC012357](https://doi.org/10.1002/2016JC012357). URL: <https://onlinelibrary.wiley.com/doi/10.1002/2016JC012357>.
- Pollard, Raymond T., Peter B. Rhines, and Rory O. R. Y. Thompson (1973). "The deepening of the wind-Mixed layer." In: *Geophysical Fluid Dynamics* 4.4, pp. 381–404. ISSN: 0016-7991. DOI: [10.1080/03091927208236105](https://doi.org/10.1080/03091927208236105). URL: <https://www.tandfonline.com/doi/full/10.1080/03091927208236105>.
- Price, James F. and Miles A. Sundermeyer (1999). "Stratified Ekman layers." In: *Journal of Geophysical Research: Oceans* 104.C9, pp. 20467–20494. ISSN: 01480227. DOI: [10.1029/1999JC900164](https://doi.org/10.1029/1999JC900164). URL: <http://doi.wiley.com/10.1029/1999JC900164>.
- Price, James F., Robert A. Weller, and Robert Pinkel (1986). "Diurnal cycling: Observations and models of the upper ocean response to diurnal heating, cooling, and wind mixing." In: *Journal of Geophysical Research* 91.C7, p. 8411. ISSN: 0148-0227. DOI: [10.1029/JC091iC07p08411](https://doi.org/10.1029/JC091iC07p08411). URL: <http://doi.wiley.com/10.1029/JC091iC07p08411>.
- Reffray, G., R. Bourdalle-Badie, and C. Calone (2015). "Modelling turbulent vertical mixing sensitivity using a 1-D version of NEMO." In: *Geoscientific Model Development* 8.1, pp. 69–86. ISSN: 1991-9603. DOI: [10.5194/gmd-8-69-2015](https://doi.org/10.5194/gmd-8-69-2015). URL: <https://gmd.copernicus.org/articles/8/69/2015/>.
- Rivera-Rosario, Gustavo, Peter J. Diamessis, Ren-Chieh Lien, Kevin G. Lamb, and Greg N. Thomsen (2020). "Formation of Recirculating Cores in Convectively Breaking Internal Solitary Waves of Depression Shoaling over Gentle Slopes in the South China Sea." In: *Journal of Physical Oceanography* 50.5, pp. 1137–1157. ISSN: 0022-3670. DOI: [10.1175/JPO-D-19-0036.1](https://doi.org/10.1175/JPO-D-19-0036.1). URL: <https://journals.ametsoc.org/view/journals/phoc/50/5/jpo-d-19-0036.1.xml>.
- Smyth, William D. and James N. Moum (2000). "Length scales of turbulence in stably stratified mixing layers." In: *Physics of Fluids* 12.6, pp. 1327–1342. ISSN: 1070-6631. DOI: [10.1063/1.870385](https://doi.org/10.1063/1.870385). URL: <http://aip.scitation.org/doi/10.1063/1.870385>.

- Soloviev (2006). *The Near-Surface Layer of the Ocean*. Vol. 31. Atmospheric and Oceanographic Sciences Library. Dordrecht: Kluwer Academic Publishers. ISBN: 1-4020-4052-0. DOI: [10.1007/1-4020-4053-9](https://doi.org/10.1007/1-4020-4053-9). URL: <http://link.springer.com/10.1007/1-4020-4053-9>.
- Thorpe, S. A. (2005). *The Turbulent Ocean*. Cambridge University Press. ISBN: 9780521835435. DOI: [10.1017/CB09780511819933](https://doi.org/10.1017/CB09780511819933). URL: <https://www.cambridge.org/core/product/identifier/9780511819933/type/book>.
- (2007). *An Introduction to Ocean Turbulence*. Cambridge: Cambridge University Press. ISBN: 9780511801198. DOI: [10.1017/CB09780511801198](https://doi.org/10.1017/CB09780511801198). URL: <http://ebooks.cambridge.org/ref/id/CB09780511801198>.
- Umlauf, Lars and Hans Burchard (2005). “Second-order turbulence closure models for geophysical boundary layers. A review of recent work.” In: *Continental Shelf Research* 25.7-8, pp. 795–827. ISSN: 02784343. DOI: [10.1016/j.csr.2004.08.004](https://doi.org/10.1016/j.csr.2004.08.004). URL: <https://linkinghub.elsevier.com/retrieve/pii/S0278434304003152>.
- Voke, Peter R. and Zhiyin Yang (1995). “Numerical study of bypass transition.” In: *Physics of Fluids* 7.9, pp. 2256–2264. ISSN: 1070-6631. DOI: [10.1063/1.868473](https://doi.org/10.1063/1.868473). URL: <http://aip.scitation.org/doi/10.1063/1.868473>.
- Windt, Christian, Josh Davidson, and John Ringwood (2020). “Investigation of Turbulence Modeling for Point-Absorber-Type Wave Energy Converters.” In: *Energies* 14.1, p. 26. ISSN: 1996-1073. DOI: [10.3390/en14010026](https://doi.org/10.3390/en14010026). URL: <https://www.mdpi.com/1996-1073/14/1/26>.
- Wu, Jinlong, Heng Xiao, Rui Sun, and Qiqi Wang (2019). “Reynolds-averaged Navier–Stokes equations with explicit data-driven Reynolds stress closure can be ill-conditioned.” In: *Journal of Fluid Mechanics* 869, pp. 553–586. ISSN: 0022-1120. DOI: [10.1017/jfm.2019.205](https://doi.org/10.1017/jfm.2019.205). URL: <https://www.cambridge.org/core/product/identifier/S0022112019002052/type/journal-article>.
- Zikanov, OLEG, DONALD N. SLINN, and MANHAR R. DHANAK (2003). “Large-eddy simulations of the wind-induced turbulent Ekman layer.” In: *Journal of Fluid Mechanics* 495, S0022112003006244. ISSN: 00221120. DOI: [10.1017/S0022112003006244](https://doi.org/10.1017/S0022112003006244). URL: <http://www.journals.cambridge.org/abstract/S0022112003006244>.